Materials and Design 201 (2021) 109469

Contents lists available at ScienceDirect

Materials and Design

journal homepage: www.elsevier.com/locate/matdes

Multiaxial fatigue behaviour of maraging steel produced by selective laser melting

R. Branco [a,*], J.D. Costa [a], J.A. Martins Ferreira [a], C. Capela [a,b], F.V. Antunes [a], W. Macek [c]

[a] University of Coimbra, CEMMPRE, Department of Mechanical Engineering, Coimbra, Portugal
[b] ESTG, Department of Mechanical Engineering, Instituto Politécnico de Leiria, Leiria, Portugal
[c] University of Occupational Safety Management, Bankowa 8, 40-007 Katowice, Poland

HIGHLIGHTS

- Multiaxial fatigue behaviour was significantly affected by the bending moment to the torsion moment ratio.
- Un-melted regions at surface and subsurface were the main cause of fatigue crack initiation at the notch.
- Fatigue crack initiation sites and fatigue crack angles were predicted from the first principal stress field.
- Multiaxial fatigue life was successfully predicted using an uniaxial one-parameter damage law.

GRAPHICAL ABSTRACT

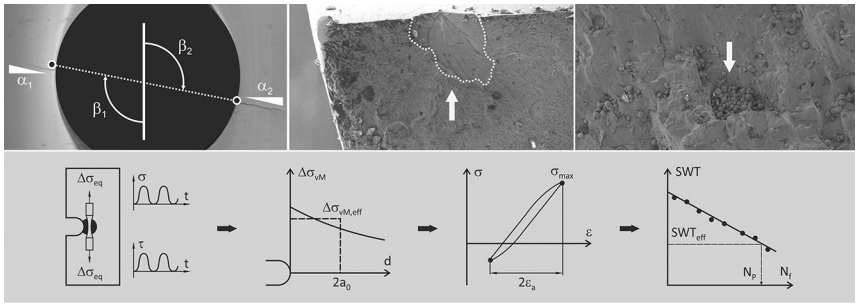

ARTICLE INFO

Article history:
Received 21 July 2020
Received in revised form 19 December 2020
Accepted 9 January 2021
Available online 13 January 2021

Keywords:
Multiaxial fatigue
Bending-torsion
Maraging steel
18Ni300 steel
Selective laser melting
Strain energy density
SWT damage parameter
Theory of critical distances
Notch plasticity correction

ABSTRACT

This paper studies the multiaxial fatigue behaviour of maraging steel samples produced by selective laser melting. Hollow cylindrical specimens with transverse circular holes are subjected to different in-phase bending-torsion loading scenarios. Fatigue crack initiation sites and fatigue crack angles are predicted from the first principal stress field. Fatigue lifetime is computed using a straightforward approach, based on a one-parameter damage law, developed via uniaxial low-cycle fatigue tests. The cyclic plasticity at the notch-controlled process zone is accounted for by combining the equivalent strain energy density concept and the theory of critical distances within a linear-elastic framework. Regardless of the multiaxial loading scenario, experimental observations and predicted lives are very well correlated.

* Corresponding author.
E-mail address: ricardo.branco@dem.uc.pt (R. Branco).

https://doi.org/10.1016/j.matdes.2021.109469

1. Introduction

Maraging steels are a special class of advanced high-strength steels, widely used in the aircraft, aerospace, military, offshore, subsea, tooling and moulding industries [1,2], due to the combination of unusual properties, namely high-strength, toughness, ductility and weldability along with dimensional stability. This special class of steels, whose microstructure is formed by a cubic martensitic matrix, is hardened by finely dispersed nanometer-sized precipitates of intermetallic compounds, formed from a metallurgical reaction involving no carbon, which seriously hampers the movements of dislocations and, thereby, promotes strengthening by precipitation hardening processes [3,4].

Because of their martensitic matrix, these materials require a rapid quench from the austenitic region to temperatures below the martensite start temperature, which makes them particularly suited for the selective laser melting technology [4,5]. This fact can be explained by the small size of the melt pool that leads to very high cooling rates. On the other hand, the cyclic reheating experienced by the material may trigger the nucleation of hardening precipitates without the need of additional heat treatments [4]. Last but not least, the geometrically complex shapes and the relatively reduced quantities associated with the typical application areas are two other important requirements that can be met by this process [4,5].

Selective laser melting is a very popular but unequivocally complex technique for metal processing that creates fully-functional components, directly from three-dimensional digital models, by successive deposition of thin layers of material [4,6]. Due to the nature of this additive manufacturing process, products are prone to different types of anomalies (e.g. porosities, inclusions, voids, cavities, micro-cracks, shrinkage, lack of fusion, excessive roughness, etc.) increasing the uncertainty regarding the mechanical behaviour. Therefore, a good understanding of structural integrity under monotonic and cyclic loading is pivotal to extend the field of application and develop more sophisticated products.

The interconnection between the monotonic properties, the process parameters and the microstructural features in materials processed by additive manufacturing has been extensively investigated. The recent review papers by Fayazfar et al. [7], by Bajaj et al. [8], and by Mooney et al. [9] provide an overview of this triangular dependency and define general guidelines to achieve fully dense parts. Concerning maraging steels, there is a considerable number of studies on the process-microstructure-property relationship. We can mention, for instance, the influence of fabrication parameters [10–13], alloy design [14,15], thermal cycles [16,17], post-processing treatments [18–20], surface roughness [21,22], and chemical composition [23], among others.

Although the above-mentioned relationships are relatively clear, the literature on the mechanical behaviour under cyclic loading is less abundant and has been mainly focused on uniaxial loading scenarios. Furthermore, the development of tailor-made methods for fatigue life assessment is yet in an embryonic stage. As far as the 18Ni300 maraging steel is concerned, to the best of our knowledge, there are no studies dealing with multiaxial loading. Multiaxial loading is a critical issue in mechanical design that requires tuned engineering approaches. Therefore, the present paper aims to fill these gaps. Firstly, we study the multiaxial fatigue behaviour of 18Ni300 steel parts manufactured by selective laser melting (SLM), and then we develop a multiaxial fatigue model.

The paper is organised as follows: Section 2 provides a review on the recent advances in fatigue behaviour of maraging steels produced by additive manufacturing. Section 3 presents the multiaxial fatigue model developed in this research. Section 4 gathers information on the experimental fatigue program and describes the numerical model developed to evaluate the cyclic plasticity at the notch-controlled process zone. Section 5 presents the main outcomes on the multiaxial fatigue campaign and the multiaxial fatigue life prediction. Finally, the paper ends with a summary of the most relevant findings.

2. Literature review

According to the open literature, the first studies on the fatigue behaviour of 18Ni300 steel produced by additive manufacturing were conducted by Croccolo et al. [24], who analysed the effect of building orientation (0°, 45° and 90°) on fatigue strength under rotating bending fatigue. Regardless of the specimen orientation, the fatigue strength was nearly the same, approximately 30% of the ultimate tensile strength, which was attributed to the beneficial effect of aging and shot-peening treatments that reduced the level of anisotropy. The effect of post-processing treatments on the high-cycle fatigue response was revisited in subsequent papers [25–28]. Overall, the fatigue strength was considerably incremented, roughly 40% of the ultimate tensile strength, when the specimens were shot-penned, heat-treated, and machined. The advantages of other post-processing treatments on fatigue performance, namely sand blasting and glass blasting, were clearly demonstrated in the recent papers by Elangeswaran et al. [29] and Bouzakis et al. [30].

Martins Ferreira et al. [31–33] investigated the fatigue behaviour of 18Ni300 steel samples fabricated via selective laser melting subjected to uniaxial pulsating loading. These authors reported that the stress-life response under load-control mode was significantly different from that under displacement-control mode [32]. In the former case, particularly at lower stress levels, fatigue lives were increasingly higher than those of the latter case. Nevertheless, at higher stress levels, no significant differences were observed. Another interesting finding was that the fatigue strength of fully sintered parts and hybrid parts (i.e. half printed by selective laser melting and half made of conventional steel) was similar for shorter lives, but quite different for longer lives [32,33]. At longer lives, hybrid samples exhibited a lower fatigue performance.

The same research team, in a recent study about the effect of single and multiple overloads on fatigue crack propagation in as-built and heat-treated samples concluded that the heat-treatment reduced the crack retardation after the overload and suppressed the existence of crack closure in the transient regime, which was associated with the strong bifurcation phenomenon caused by the overload [34]. Furthermore, the heat-treated samples led to lower fatigue crack growth rates, not only in the stable regime, but also near threshold. This behaviour was explained by the microstructural changes, the hardness increase, and the residual stress reduction caused by the heat-treatment. The microstructure modification also had an important role on crack paths and failure mechanisms. In another study dealing with the fatigue crack growth of hybrid samples subjected to single overloads, plasticity-induced crack closure was not observed, which was explained by bifurcation phenomena [35].

The fatigue crack growth rates in heat-treated compact-tension specimens were also measured by Suryawanshi et al. [36]. Nevertheless, the focus of this study was put on the printing orientation. An important conclusion was that no significant anisotropy was detected in the mechanical properties. The reasons for that were the strong intra-layer bonding and the absence of a dominant texture. Moreover, either for the specimens with cracks machined parallelly or transversally to the building direction, the fatigue crack growth rates were similar. Another finding was that the SLM maraging steel after aging exhibited identical fatigue crack growth characteristics to the same grade produced by conventional manufacturing.

Similarly, Meneghetti et al. [37,38] found that the axial fatigue response of both as-built and age hardening heat-treated samples, at shorter lives, was not particularly affected by the building direction. Nevertheless, at longer lives, the fatigue strength of the vertically built specimens was progressively higher than that of those built in the horizontal direction. On the other hand, when compared to the wrought material, both orientations led to lower fatigue strengths. This conclusion is in line with the work of Damon et al. [39] who reported a considerable reduction of fatigue strength (30–50% lower) when compared to

that of the conventionally cast material, either at high temperature or in air.

Gatto et al. [40] addressed the effect of cross-contamination of the raw material on fatigue resistance of heat-treated specimens processed by powder bed fusion. One important outcome was that while the static properties were not affected by the presence of contaminants, the axial fatigue response was significantly altered, even in the cases that the average chemical composition was within the nominal range. However, in the absence of contamination, fatigue lives were similar to those of the forged steel. This detrimental effect, also observed for extremely localised anomalies, suggests that the standard quality control methods used in the analysis of raw materials must be rethought, particularly in critical applications, whose failure can cause more than a merely commercial damage.

Regarding the determination of fatigue properties, additive manufacturing has opened new perspectives. Santos et al. [41] developed a novel specimen with an internal circular crack to evaluate the fatigue crack growth rates in vacuum. The most interesting features are that the internal crack is exposed to a vacuum-like environment, as oxidation and gas absorption are negligible; the crack front, due to the circular configuration, is dominated by plane strain state; and the technical equipment required to perform the tests is considerably simplified. Douellou et al. [42,43] built up a statistical-based model, by using infrared thermography, to determine the fatigue resistance of laser power bed fusion parts. In this approach, the mechanical dissipation associated with the fabrication strategy is linked to the fatigue damage.

The fatigue behaviour under variable-amplitude loading has been investigated by a few researchers. Martins Ferreira et al. [32,34] studied the fatigue performance of sintered and hybrid specimens subjected to block loading sequences. Although conservative for longer lives, Miner's law along with conventional S–N diagrams obtained at the same stress ratio were capable of estimating the fatigue lifetime. Dealing with the same loading scenarios, Branco et al. [44] demonstrated that the Miner's law combined with a one-paramater damage law defined from uniaxial fully-reversed strain-controlled tests could successfully predict the fatigue durability. The concept was later simplified, being the damage-life relationship re-engineered from only two conventional low-cycle fatigue tests, without affecting the predictive capabilities of the proposed approach [45].

As far as the low-cycle fatigue regime is concerned, very limited work has been reported in the literature [46,47]. Branco et al. [47] showed that the SLM maraging steel, in the as-built condition, exhibits a slight cyclic strain-softening behaviour and that the total strain energy density is an adequate parameter to correlate the fatigue damage with the life expectancy [46]. Mooney et al. [48] found that the cyclic elastic-plastic response under fully-reversed strain-controlled conditions can be modelled via a kinematic hardening rule in conjunction with either an isotropic yield function or an anisotropic yield function. Nevertheless, the latter offers a more representative description of the mechanical behaviour.

The application of advanced numerical methods to study the fatigue behaviour of this alloy produced by additive manufacturing has been another line of research. Antunes et al. [48–51] studied the fatigue crack growth based on the plastic crack-tip opening displacement (CTOD) in compact tension specimens subjected to constant-amplitude loading. Similar to other conventional alloys, a well-defined relationship between the fatigue crack growth rate and the plastic CTOD, independent of the stress ratio and the specimen thickness, was found. Based on the finite element method, Ebrahimi et al. [52] designed a mixed analytical-numerical approach to determine the fatigue life in hybrid samples produced by direct metal laser sintering. The innovative aspect is the possibility to account for the residual stress fields generated during the welding process.

To conclude this section, we would like to mention the review papers by Fayazfar et al. [7] and by Afkhami et al. [53] where the reader can find important information on the mechanical properties and the fatigue behaviour of different additively manufactured alloys. The former provides an overview of the triangular relationship among process parameters, microstructural features, and mechanical properties and the focus is put on the SLM, laser powder-fed, and binder jetting processes. The latter presents a detailed analysis of the fatigue characteristics in steels processed by SLM and identifies the potential research directions. One of these directions is the fatigue behaviour of SLM steels under "*multiaxial cyclic loading*" which remains unstudied. According to the authors, "*this gap might result in the lack of understanding of the correct damage mechanism and inability of having a comprehensive fatigue life prediction in industrial applications*".

3. Multiaxial fatigue life prediction model

The fatigue design of engineering components subjected to multiaxial loading histories is a complex problem. Its non-trivial nature has inspired the development of different prediction proposals, which are usually organised into stress-based, strain-based, energy-based, and critical plane-based models [54–57]. Another challenging issue associated with the design against fatigue of critical engineering components is the notch effect [58,59]. Currently, there are different theories to deal with the notch effect. Among the most successful approaches, we can mention those based on the strain energy density and those based on the critical distance. A comprehensive review on the modelling of the notch effect in fatigue problems has been recently published by Liao et al. [60]. In general, the most efficient multiaxial fatigue models require a huge number of material constants and complex computational simulations, making the process time-consuming and expensive.

The proposed fatigue life prediction model aims to solve the above-mentioned issues. Two fundamental premises are assumed as a starting point: (1) regardless of the geometric discontinuity, fatigue life is the same, if the stress-strain histories at the initiation sites are similar; and (2) fatigue failure occurs when a critical value of damage is reached at the initiation site. The modus operandi is divided into two main stages. The first stage, represented in Fig. 1, is devoted to the material characterisation, and encompasses the determination of a one-parameter damage law, the calculation of fatigue strength, and the definition of stress intensity factor range threshold.

As far as the damage law is concerned, the selected fatigue quantifier is the well-known Smith-Watson-Topper (SWT) parameter, written in the form [61]:

$$SWT = \varepsilon_a \sigma_{max} \tag{1}$$

where ε_a is the strain amplitude, and σ_{max} is the maximum stress. In this research, the correlation between the fatigue damage and the number of cycles to failure is defined from a series of uniaxial low-cycle fatigue tests conducted under fully-reversed strain-control conditions [45].

The determination of the fatigue strength and the stress intensity factor range threshold allows the definition of the material characteristic size [62]:

$$a_0 = \frac{1}{\pi}\left(\frac{\Delta K_{th}}{\Delta \sigma_0}\right)^2 \tag{2}$$

where ΔK_{th} is the stress intensity factor range threshold, and $\Delta\sigma_0$ is the fatigue limit stress range. Both variables must be assessed at the same stress ratio of the notched member. The former can be evaluated using cracked standard specimens under load-control mode, while the latter can be determined from unnotched specimens under stress-controlled conditions.

The second stage, represented in Fig. 2, aims at estimating the fatigue lifetime under multiaxial loading histories for the notched members. The proposed procedure starts with the reduction of the multiaxial stress state to an uniaxial stress state at the notch-controlled process zone using the equivalent von Mises stress range (Fig. 2(a)). Then, the

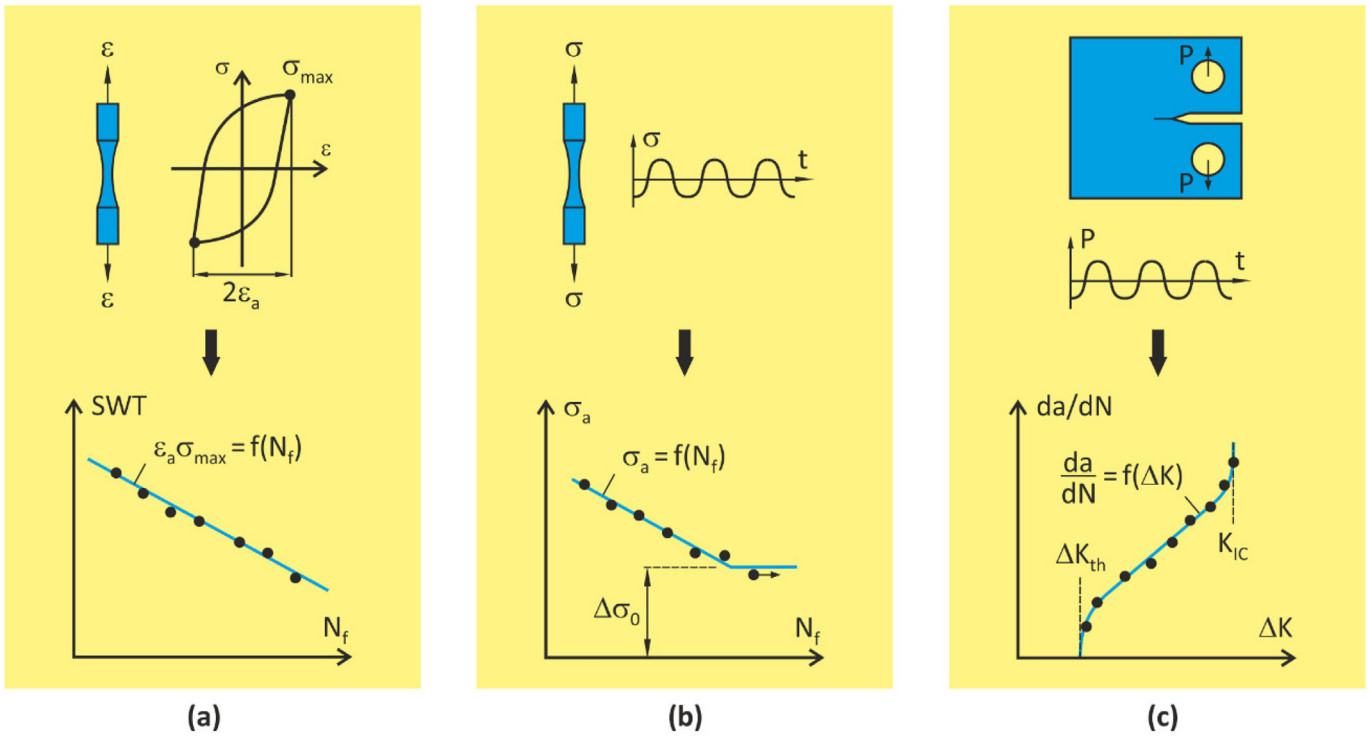

Fig. 1. Material characterisation: (a) one-parameter damage law; (b) fatigue strength; and (c) stress intensity factor range threshold (ε is the strain; ε_a is the strain amplitude; ΔK is the stress intensity factor range; ΔK_{th} is the stress intensity factor range threshold; $\Delta\sigma_0$ is the fatigue limit stress range; σ is the stress; σ_a is the stress amplitude; σ_{max} is the maximum stress; da/dN is the fatigue crack growth rate; K_{IC} is the fracture toughness; P is the load; SWT is the Smith-Watson-Topper parameter; and t is time).

local stress distribution is averaged by applying the line method of the theory of critical distances [63,64], as schematised in Fig. 2(b). After that, based on the effective von Mises stress range, a representative hysteresis loop is generated through the equivalent strain energy density concept (Fig. 2(c)). Finally, the corresponding value of the SWT damage parameter is inserted into the one-parameter damage law to estimate the associated fatigue life (Fig. 2(d)).

4. Materials and methods

4.1. Material and specimens

The material selected for all experiments performed in this study was the 18Ni300 maraging steel produced by selective laser melting.

Table 1
Chemical composition of AISI 18Ni300 (wt%).

C	Ni	Mn	Co	Mo	Ti	Al	Cr	P	Si	Mn	Fe
0.01	18.2	0.65	9.0	5.0	0.6	0.05	0.3	0.01	0.1	0.04	Balance

Its nominal chemical composition and its main mechanical properties are summarised in Table 1 and Table 2, respectively. The experimental fatigue campaign comprised multiaxial fatigue tests, low-cycle fatigue tests, high-cycle fatigue tests, and fatigue crack growth tests. All tests were carried out using a conventional servo-hydraulic testing machine, in air, at room temperature, and with sinusoidal waveforms.

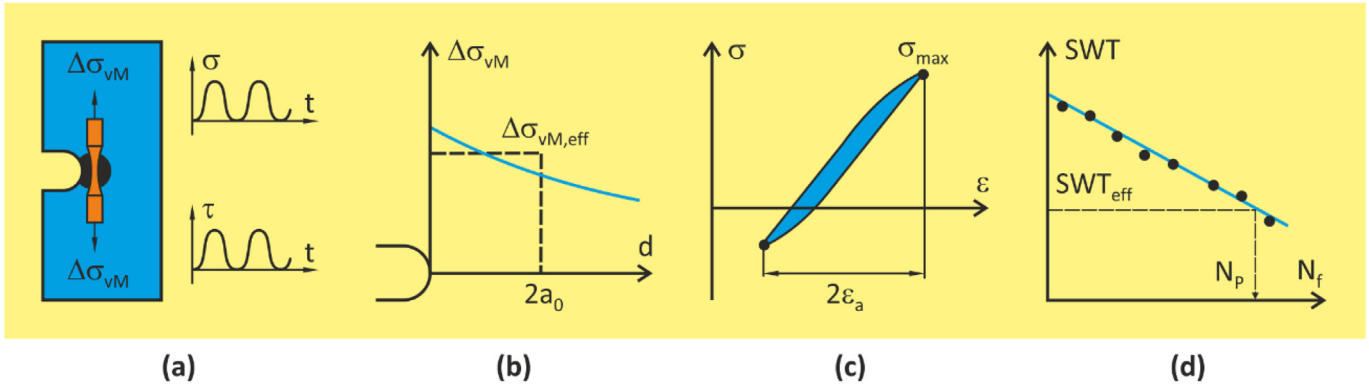

Fig. 2. Fatigue life prediction: (a) reduction of multiaxial stress state to an equivalent uniaxial stress state; (b) calculation of an effective stress range; (c) generation of a cyclic hysteresis loop; and (d) estimation of fatigue lifetime (ε is the strain; ε_a is the strain amplitude; $\Delta\sigma_{vM}$ and $\Delta\sigma_{vM,eff}$ are the equivalent von Mises stress range and its effective value; σ and τ are the normal and shear stresses; a_0 is the material characteristic size; d is the distance from the notch root; N_f and N_p are the number of cycles to failure and the predicted lifetime; t is time; and SWT and SWT_{eff} are the Smith-Watson-Topper parameter and its effective value).

Table 2
Mechanical properties of AISI 18Ni300.

Property	Value
Porosity (%)	0.74
Density (g/m^3)	7.42
Poisson's ratio	0.33
Young's modulus (GPa)	168
Tensile strength (MPa)	1147
Yield strength (MPa)	910
Strain at failure (%)	5.12
Cyclic hardening coefficient (MPa)	1921.21
Cyclic hardening exponent	0.110

Table 3
Summary of the multiaxial fatigue tests.

B/T	2	2	2	1	1	1	2/3	2/3
σ_a (MPa)	78.3	79.6	95.5	66.3	79.6	95.5	55.3	79.6
σ_m (MPa)	86.1	87.6	105.1	73.0	87.6	105.1	60.8	87.6
N_i (cycles)	35,115	75,516	20,037	52,883	32,677	7947	84,204	8514

B/T = 2 ($\sigma_a/\tau_a = 4, \sigma_m/\tau_m = 4$); B/T = 1 ($\sigma_a/\tau_a = 2, \sigma_m/\tau_m = 2$); B/T = 2/3 ($\sigma_a/\tau_a = 4/3, \sigma_m/\tau_m = 4/3$).

The specimen geometries, exhibited in Fig. 3, were fabricated in a vertical orientation, on the base plate, using a Concept Laser M3 linear printing system equipped with a Nd:YAG fibre laser. The building strategy comprised the deposition of 40 μm thick layers, with a hatch spacing of 100 μm, at a scan speed of 200 mm/s. After the additive manufacturing process, specimens were machined and polished to a scratch-free condition by means of progressively finer grades of silicon carbide papers (P600-grit, P1200-grit, and P2500-grit) followed by a 6-μm diamond water-based polishing paste.

4.2. Multiaxial fatigue tests

Multiaxial fatigue tests were carried out under in-phase constant-amplitude pulsating loading conditions (i.e. with a stress ratio, R_σ, equal to 0) using 150 mm-long hollow cylindrical specimens with a 5 mm-diameter transversal hole (see Fig. 3(a)). The outside diameter was equal to 16 mm, while the internal diameter was equal to 9 mm. The loading scenarios, complied in Table 3, encompassed three bending moment to torsion moment ratios (B/T), respectively equal to 2, 1 and 2/3, and different nominal stress amplitudes. A high-resolution digital camera was used to detect the crack initiation sites and to track the crack paths. Images were periodically recorded with sampling rates between 1000 and 5000 cycles.

After the multiaxial fatigue tests, fracture surfaces were examined by scanning electron microscopy, model Zeiss Merlin Gemini II, to identify the main damage micro-mechanisms and by optical three-dimensional focus-variation microscopy, model Alicona InfiniteFocus G4, to characterise the surface morphology. Topography data processing and calculations were done on the basis of ISO 25178 standard by using MountainsMap surface metrology software [65,66]. Surface textures were characterised by Abbott-Firestone curves, constructed by finding the distribution of the heights of peaks and valleys in the areas [56].

4.3. Low-cycle fatigue tests

Low-cycle fatigue tests were conducted under fully-reversed strain-controlled conditions ($R_\varepsilon = -1$) following the recommendations outlined in ASTM E606–19 standard. The specimen geometry (see Fig. 3(b)) had a cylindrical gauge section with a length of 19 mm

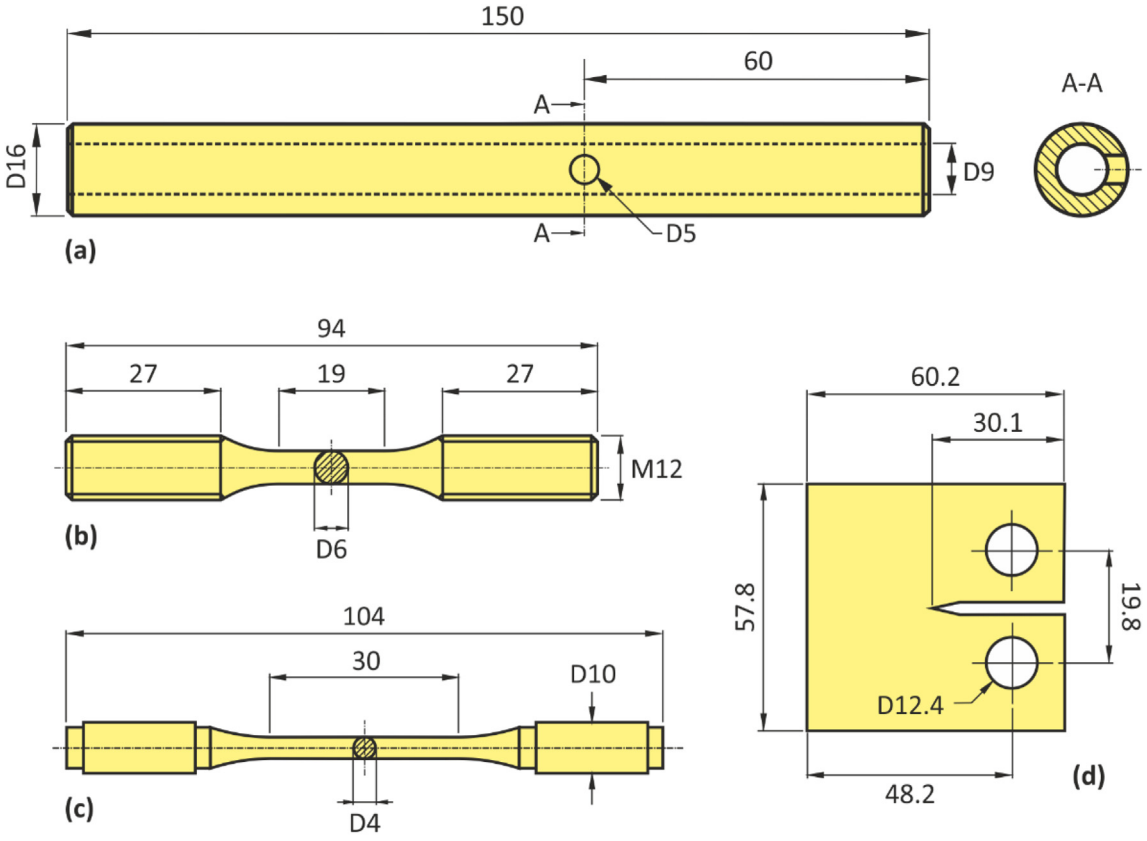

Fig. 3. Specimen geometries used in the experimental campaign: (a) multiaxial fatigue tests; (b) low-cycle fatigue tests; (c) high-cycle fatigue tests; and (d) fatigue crack growth tests (dimensions in millimetres).

Table 4
Summary of the low-cycle fatigue tests.

Test	1	2	3	4	5	6	7	8
$\Delta\varepsilon/2$ (%)	1.01	0.91	0.81	0.61	0.51	0.41	0.36	0.30
σ_{max} (MPa)	1005.0	990.8	1006.5	915.3	815.3	678.7	602.8	512.9
N_f (cycles)	33	64	40	129	145	1087	2399	5441

and a diameter of 6 mm. Tests were carried at a constant strain rate ($d\varepsilon/dt = 8 \times 10^{-3}$) and were stopped when the specimens separated into two pieces. The failure criterium was defined as the instant at which the maximum stress reduced 30% relative to the initial value. The cyclic stress-strain response was acquired with an axial extensometer clamped directly to the gauge section. A summary of the loading cases considered in the tests is provided in Table 4. Maximum stresses and strain amplitudes were collected for the half-life cyle.

4.4. High-cycle fatigue tests

High-cycle fatigue tests were performed in stress-control mode, according to ASTM E466–15 standard, at constant-amplitude, under pulsating loading conditions ($R_\sigma = 0$), and with a cyclic frequency between 15 and 20 Hz. The specimen, a cylindrical smooth geometry, had a total length of 104 mm and a 30 mm-long and 4 mm-diameter gauge section (see Fig. 3(c)). Tests were interrupted when the specimens reached the total failure, i.e. when the specimens separated into two pieces. Table 5 presents a brief overview of the loading scenarios considered in these tests.

4.5. Fatigue crack growth tests

Fatigue crack growth tests were conducted in accordance with ASTM E647–11 standard, under load-controlled conditions, at a constant-amplitude, with a frequency of 15–20 Hz, and a stress ratio equal to 0 ($R_\sigma = 0$). The selected geometry (see Fig. 3(d)) was a standard compact-tension specimen with a thickness of 6 mm and a width of 48.2 mm. Crack length was measured, in situ, using a travelling microscope with a magnification of forty-five times and an accuracy of 10 μm. Fatigue crack growth rates were determined by the incremental polynomial method, using five adjacent points, for crack lengths greater than 7 mm. Both the crack symmetry and the crack curvature requirements were met.

4.6. Numerical modelling and simulation

The finite element model developed to evaluate the multiaxial loading histories at the notch region of the hollow cylindrical specimens is exhibited in Fig. 4. It was created in a parametric framework, with 8-node hexahedral elements, assuming a homogeneous, linear-elastic, and isotropic material. Around the hole, an ultra-refined mesh was introduced to better describe the stress-strain gradients. At remote regions, in order to reduce the computation overhead, coarser patterns were adopted. The mesh density was defined in a step-wise manner by increasing the number of finite elements, based on the principle that the stress field tends to stabilise with the mesh refinement. The assembled model included 152,248 elements and 163,138 nodes. Regarding the ultra-refined volume surrounding the geometric discontinuity (see Fig. 4(b)), the numbers of elements and nodes were equal to 43,000 and 48,000, respectively.

Bending moments and torsion moments were generated by a single force, F, applied on the prismatic bar coupled to the specimen in the z-axis direction (see Fig. 4(a)). The bending moment to torsion moment (B/T) ratios were defined in a case-by-case basis, by changing the magnitude and the point of application of the applied force. Since the distance between the line of action of the force F and the centre of the hole (L) was constant, the relationship between the normal stress and the shear stress was defined by the following relationship:

Table 5
Summary of the high-cycle fatigue tests.

Specimen	1	2	3	4	5	6	7	8
σ_a (MPa)	150	160	180	200	224	224	280	350
N_f (cycles)	985,200	872,429	379,308	156,374	69,693	84,675	39,178	11,699

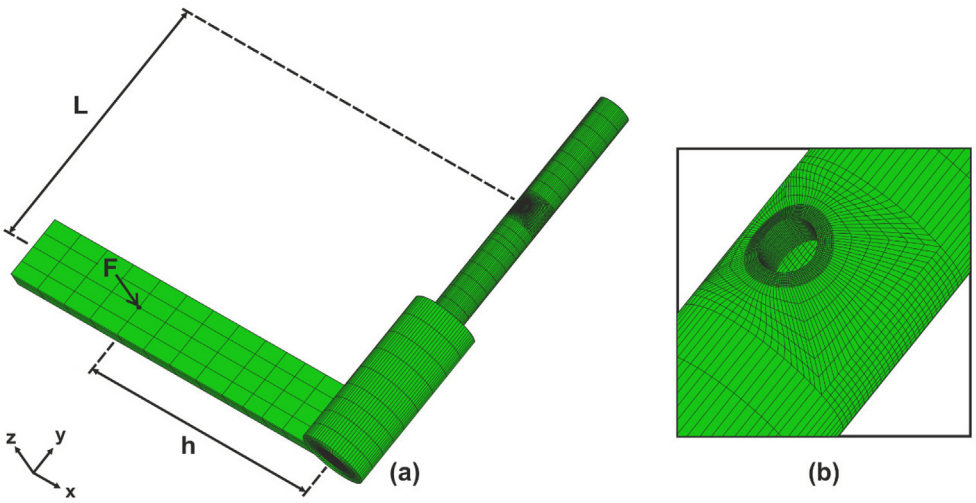

Fig. 4. Three-dimensional finite-element model developed in the present study: (a) global overview; and (b) hole region (F is the applied force; h is the distance between the line of action of the force F and main axis of the specimen; and L is distance between the line of action of the force F and the center of the hole).

$$\frac{\sigma_a}{\tau_a}=\frac{\frac{32\,F_a\,L}{\left(d_e^3-d_i^3\right)}}{\frac{16\,F_a\,h}{\left(d_e^3-d_i^3\right)}}\Rightarrow\frac{\sigma_a}{\tau_a}=\frac{2L}{h} \tag{3}$$

where σ_a is the nominal normal stress amplitude, τ_a is the nominal shear stress amplitude, F_a is the force amplitude, d_e is external diameter, d_i is the internal diameter, and h is the distance between the line of action of the force F and main axis of the specimen (see Fig. 4). At the opposite side of the specimen, the outer surface was fixed, in an extension of 30 mm from the endpoint, to simulate the boundary conditions of the gripping system.

5. Results and discussion

5.1. Multiaxial fatigue crack initiation

Multiaxial fatigue design is a complex task. One of the critical issues is the identification of the crack initiation sites. Fig. 5 shows typical examples observed in the experiments for the different B/T ratios. In this geometry, the fatigue process is characterised by the nucleation of two cracks, in diametrically opposite points, whose locations are governed by the loading scenario. It is clear from the figure that the lower the B/T ratio, the higher the initiation angles (β). This can be explained by the greater shear stress levels associated with decreasing B/T ratios. A similar behaviour was reported in the paper by Luo et al. [67] for thin-walled cylindrical specimens with a 2 mm-diameter transversal hole subjected to tensile-shear loading.

The numerical simulations confirm the aforementioned trends. Fatigue crack initiation sites can be reasonably anticipated from the nodes with maximum value of the first principal stress at the hole contour, as represented by the black dots in Fig. 5. As shown, there is a very good agreement between the experimental observations and the predicted locations. A more quantitative analysis for all multiaxial fatigue tests is presented in Fig. 6. For the sake of clarity, scatter bounds for errors of 10° are plotted (see the dashed lines). Overall, the data are well correlated, regardless of the loading case, with most of the points within the predefined limits. The average error for β_1 and β_2 was equal to 6.3° and 7.4°, respectively.

Regarding the fatigue crack initiation angles, literature suggests an important role of the loading scenario, either under in-phase or out-of-phase conditions [68–71]. The experimental measurements, as indicated in Fig. 5, show that the fatigue crack angles at the early stage of growth (α_1 and α_2) decrease with increasing values of B/T ratio. Higher B/T ratios reduce the predominance of the shear stresses and, therefore, the crack front tends to be closer to mode-I [72]. In addition, it is interesting to note that the angles of the two diametrically opposite cracks are relatively similar. Moreover, the existence of heterogeneities throughout the material, an inherent characteristic of the selective laser melting process, can explain the jagged zig-zag crack paths observed in some cases [8,35].

The fatigue angles at the early stage of crack growth were successfully predicted by accounting for the first principal direction at the crack initiation site, i.e. at the node of the hole contour with maximum value of the first principal stress. The comparison between the experimental observations and the predicted values for all multiaxial fatigue tests is plotted in Fig. 7. For the sake of clarity, scatter bounds with an error of 5° were added in the figure (see dashed lines). In fact, we can conclude that the fatigue crack angles are decreasing functions of the B/T ratio, which agrees with the literature [73,74]. Moreover, it is interesting to note that the differences between the experiments and the

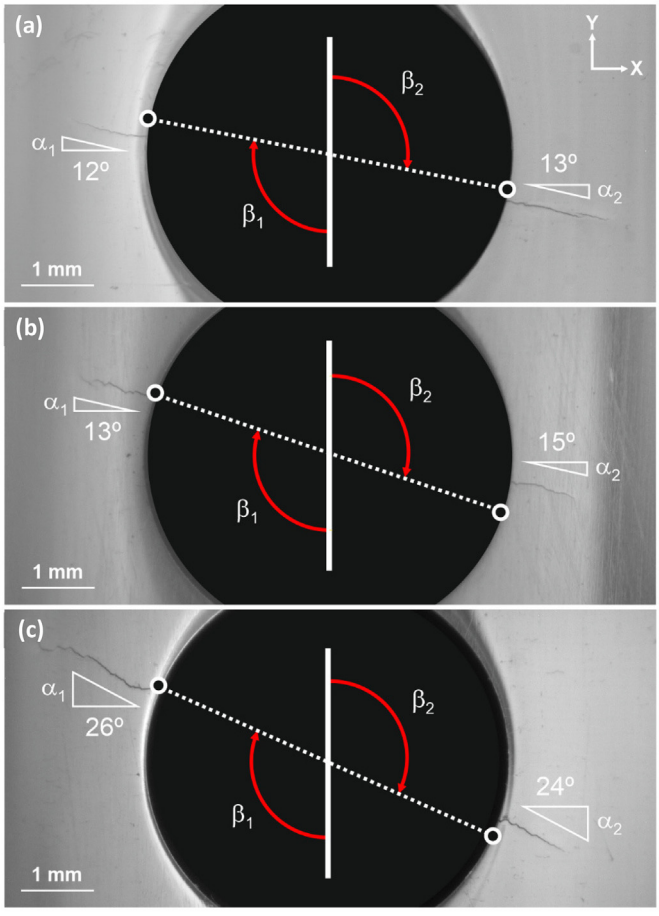

Fig. 5. Fatigue crack initiation sites: (a) B/$T = 2$; (b) B/$T = 1$; and (c) B/T = 2/3 (black dots represent the crack initiation sites predicted on the basis of the maximum value of the first principal stress at the hole contour; β_1 and β_2 represent the angles associated with the predicted initiation sites; and α_1 and α_2 represent the crack angles at the early stage of growth).

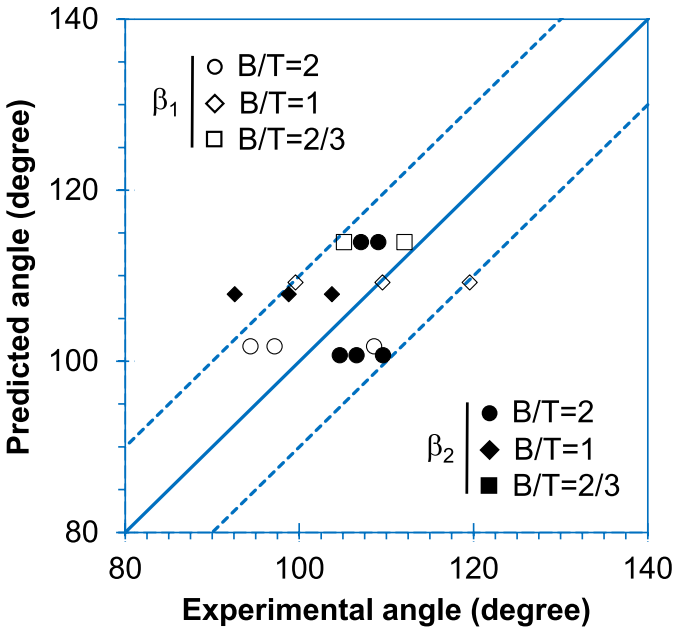

Fig. 6. Fatigue crack initiation sites: experimental observations versus numerical predictions (β_1 represent the crack on the left-hand side; β_2 represents the crack on the right-hand side; and B/T represents the bending moment to torsion moment ratio).

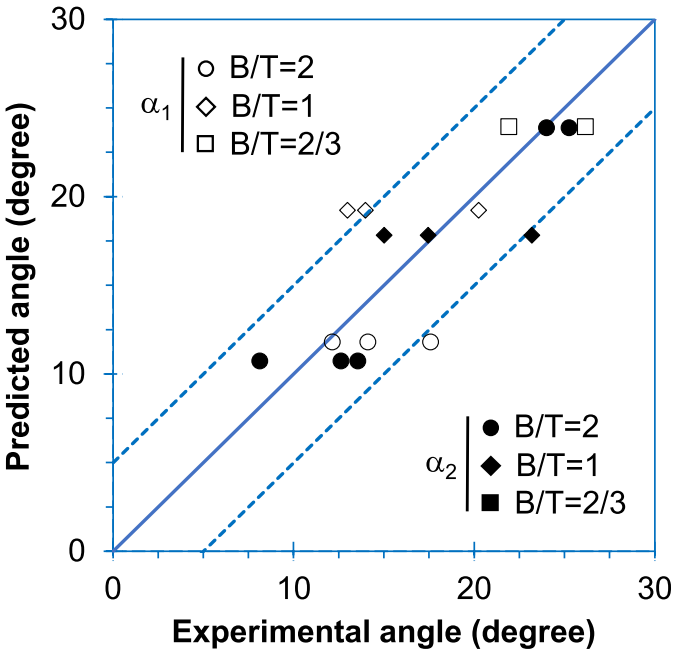

Fig. 7. Fatigue crack angles at the early stage of growth: experimental observations versus numerical predictions (α_1 represents the crack on the left-hand side; α_2 represents the crack on the right-hand side; and B/T represents the bending moment to torsion moment ratio).

simulations are particularly small. The average error for α_1 and α_2 was equal to 3.3° and 2.3°, respectively.

5.2. Multiaxial fracture surface

Fracture surfaces provide important clues on the failure mechanisms and on the origin of the structural failures. Fig. 8 exhibits typical examples of the fracture surfaces observed in the experiments, acquired by means of an optical focus-variation microscope, for different bending-torsion ratios. The analysis of the figure shows that as the B/T ratio increases, the fracture surfaces tend to be flatter, due to a lower shear stress level. Another important difference when compared to the conventional steels is the high surface roughness, which can be explained by the irregularities of the material structure [75]. In addition, the delimitation between the areas associated with cyclic loading and unstable fracture is not completely obvious.

Nevertheless, a close look at the fracture surfaces demonstrated that surface roughness increases progressively, as the crack propagates, which is expected. This outcome is summarised in the pseudo-colour images of Fig. 9, extracted from the crack initiation region, crack propagation region, and final overload region of the specimen exhibited in Fig. 8(a). Indeed, surface roughness variations become more expressive, and tend to be more random, when the fatigue crack growth rates increase. The increasingly higher levels of plastic strain underwent by the material can explain this fact. A quantitative evaluation, carried out by means of the Abbott-Firestone curves, confirms the above-mentioned trends, since the surface peaks increase during the propagation stages. Furthermore, it is interesting to note that the three height distributions are relatively similar, having the largest peaks in the middle of the histograms. The highest peaks of the three cases are in the range 270–360 μm.

A detailed examination of the fracture surfaces by SEM suggests that un-melted regions, most probably due to a lack of fusion or inadequate penetration, were the main source of crack initiation (see Fig. 10), which is common in this AM steel [9,38,47]. Crack initiation occurred from voids and cavities adjacent to the hole surface. These heterogeneities, in the presence of cyclic loads, created localised microscopic stresses, possibly larger than the yield stress, causing local plastic deformation and easing the fatigue crack initiation [35,38]. Although the samples have been machined and polished, which is likely to have reduced the surface roughness and the notch effect, remnant sub-surface defects, located close to the surface, played an important role in the crack nucleation mechanisms, and more broadly, in the entire fatigue process.

The analysis of Fig. 10 also shows that fatigue crack initiation sites were located at the hole surface, near the outer diameter of the specimen. These points are close to those predicted by the finite element simulations (i.e. the nodes with maximum value of the first principal stress identified in Fig. 11 by the black arrows). For comparison purposes, the predicted locations are plotted (white arrows) in Fig. 10(a) and (b). Although there is not a perfect match, it is reasonable to assume that these defects, due to their large size and irregular shape, acted as local stress raisers, heavily affecting the stress state, and triggering the crack nucleation close to the theoretical site, but not exactly in the predicted place.

The SEM micrographs, as exhibited in Fig. 12, revealed the presence of different types of voids and un-melted powder particles throughout the fracture surfaces. It was noted that their shapes, sizes, and distributions were quite different, which is a consequence of the SLM process. Despite inner defects can affect the fatigue behaviour, defects closer to the outer surface tend to be more detrimental. This is because crack nucleation is generally associated with the locations of higher cyclic plastic deformation. Thus, surface and sub-surface defects, due to the plane stress state condition, are subjected to more plastic deformation. In addition, since these defects are closer to the surface, they have a greater chance to cause failure, because there is a shorter distance towards an open surface.

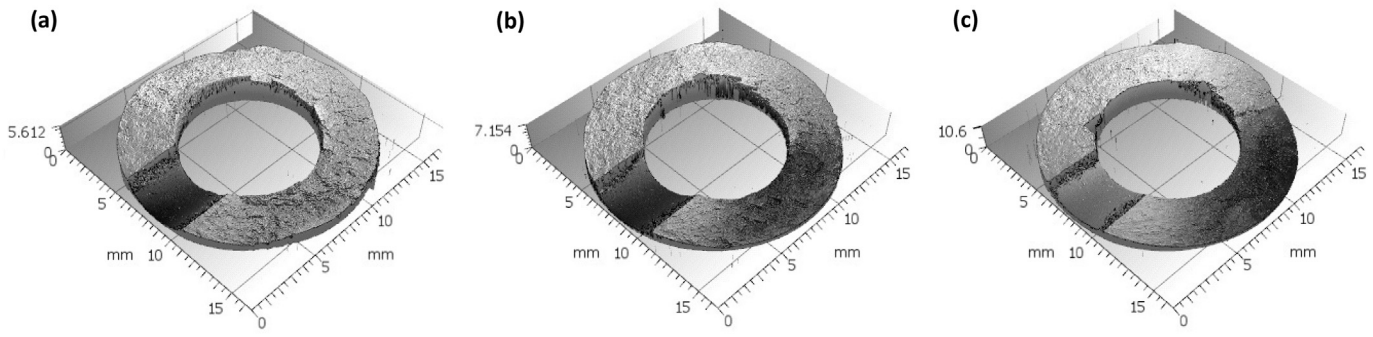

Fig. 8. Three-dimensional fracture surface topologies acquired by optical focus-variation microscopy: (a) B/T = 2; (b) B/T = 1; and (c) B/T = 2/3.

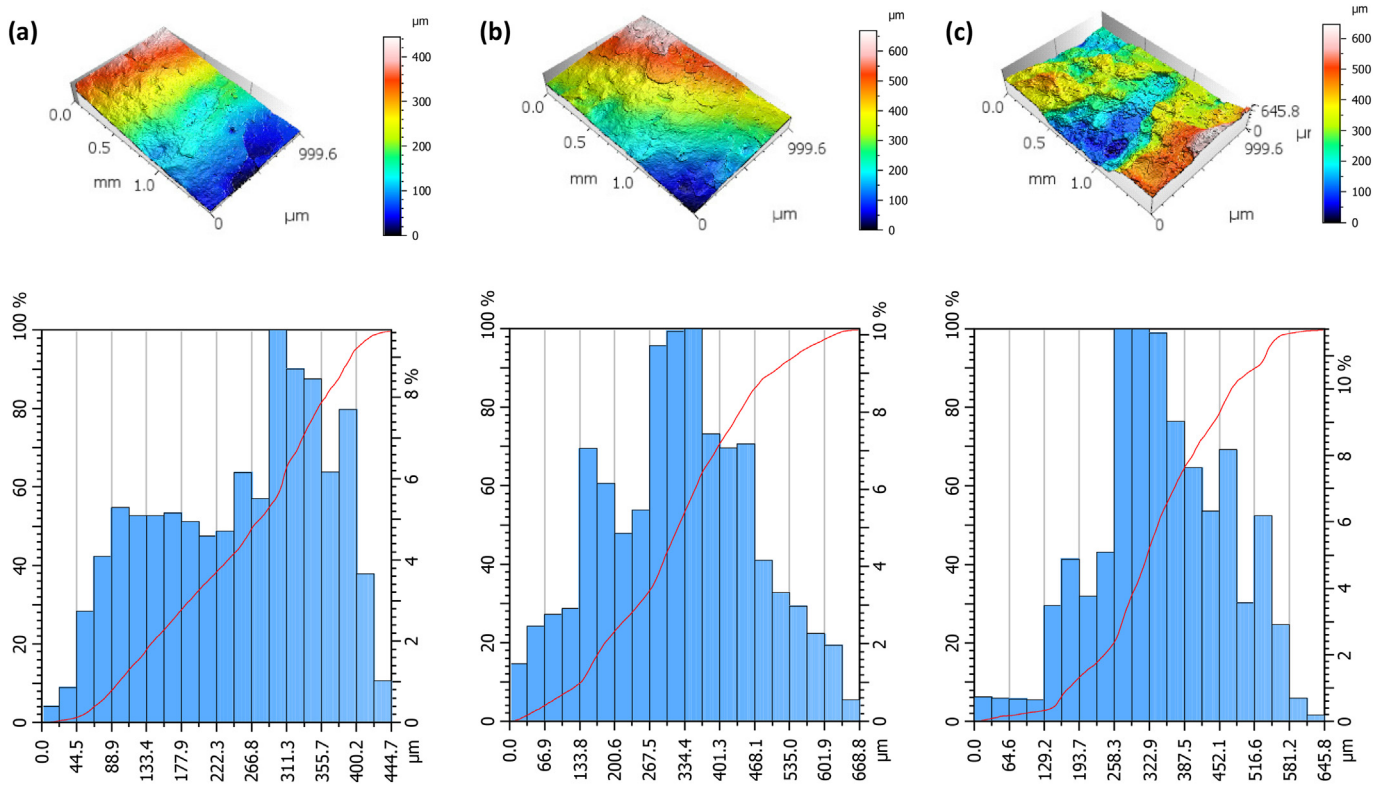

Fig. 9. Pseudo-colour views and Abbott-Firestone curves for B/T = 2: (a) crack initiation region; (b) crack propagation region; and (c) final overload region.

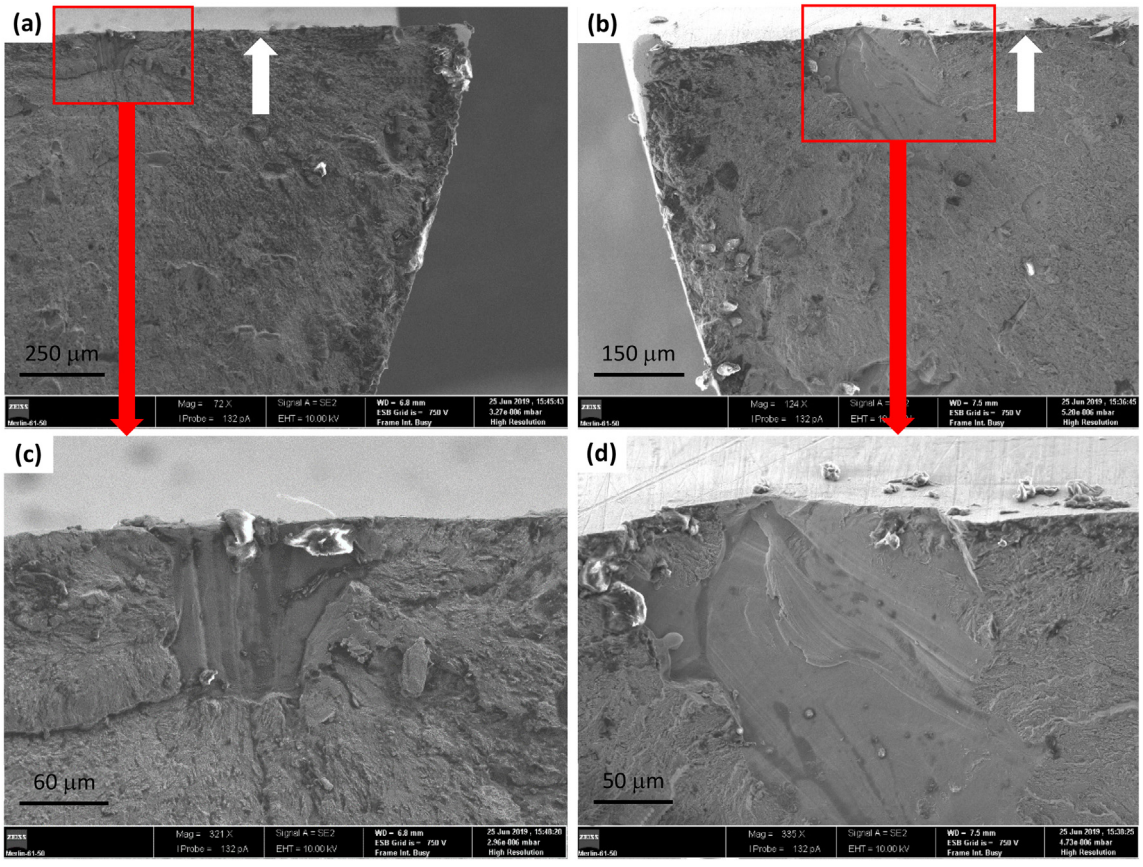

Fig. 10. SEM micrographs of crack initiation sites: (a) B/T = 2; and (b) B/*T* = 1. Magnified regions of defects close to the hole surface: (c) B/T = 2; and (d) B/T = 1. White arrows represent the predicted crack initiation sites at the hole surface.

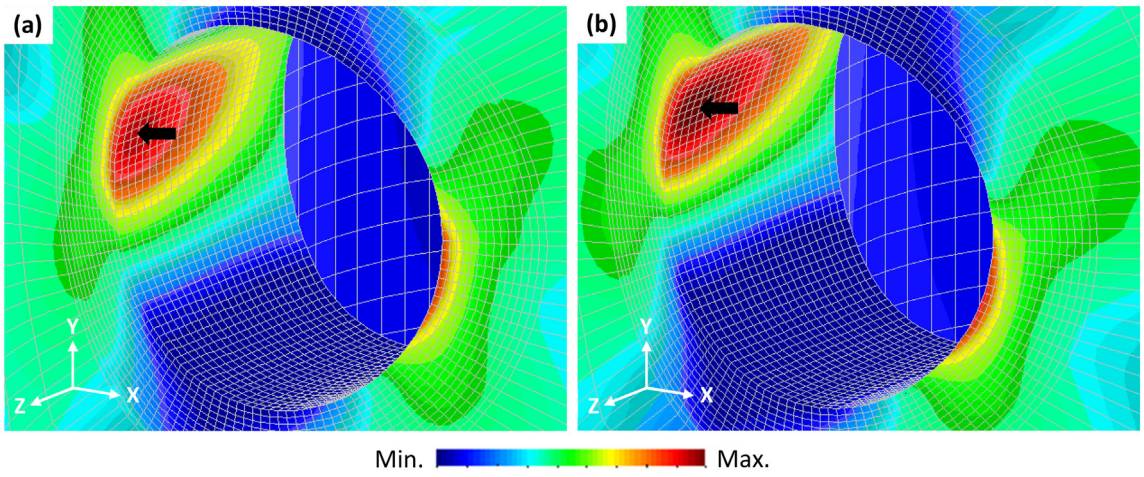

Fig. 11. First principal stress field at the hole region for: (a) B/T = 2; and (b) B/T = 1. Black arrows represent the predicted initiation site.

5.3. Multiaxial fatigue model

The multiaxial fatigue life approach utilised in this paper, as discussed in Section 3, is divided into two main stages. The first stage deals with the material characterisation, while the second is focused on the lifetime evaluation of the notched component. The two stages are addressed separately in Sections 5.3.1 and 5.3.2, respectively.

5.3.1. Material fatigue characterisation

The material characterisation, as schematised in Fig. 1, starts with the development of a one-parameter fatigue damage law. In this research, the fatigue damage is correlated with the fatigue lifetime by means of the well-known SWT damage parameter [45,62]. This relationship is established using the results of the uniaxial low-cycle fatigue tests conducted under fully-reversed strain-controlled conditions. Fig. 13 summarises the evolution of the SWT damage parameter with

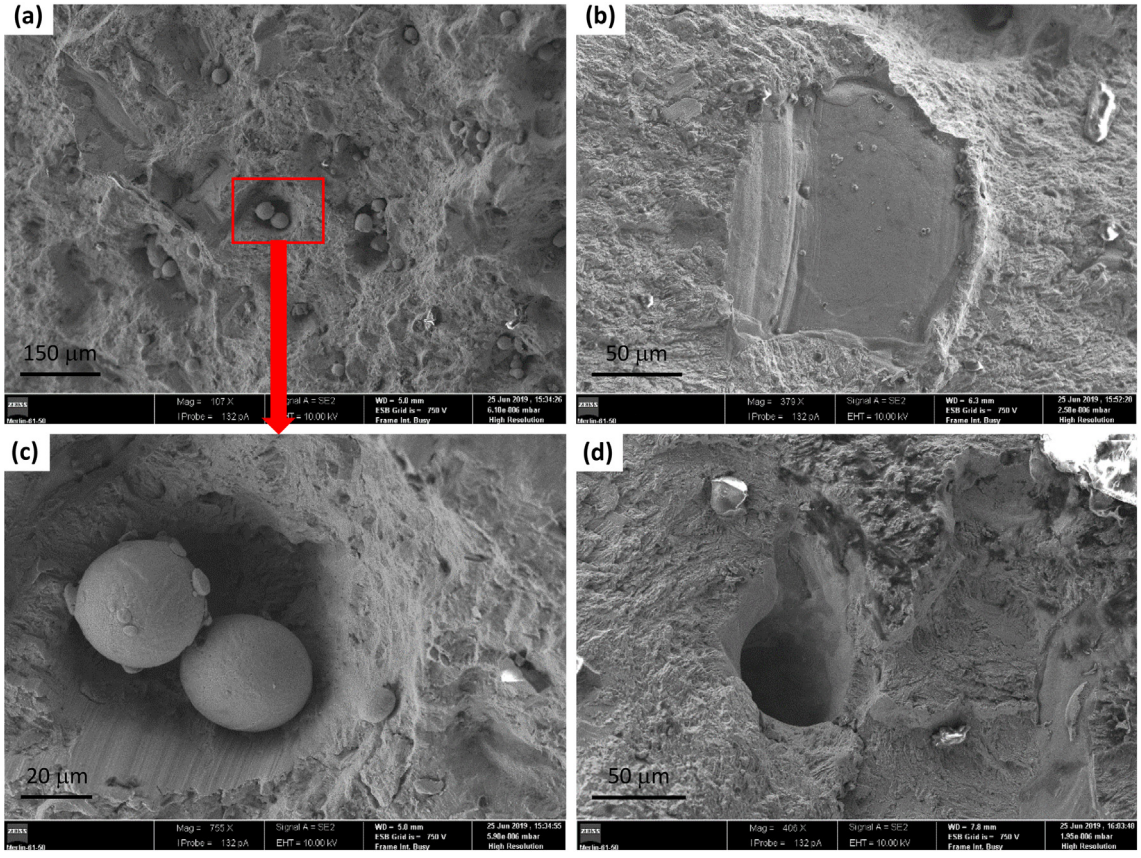

Fig. 12. Examples of processing defects found at the fracture surfaces in the SEM analysis: (a) un-melted powder particles; (b) lack of fusion; (c) magnification of un-melted powder particles; and (d) an internal void.

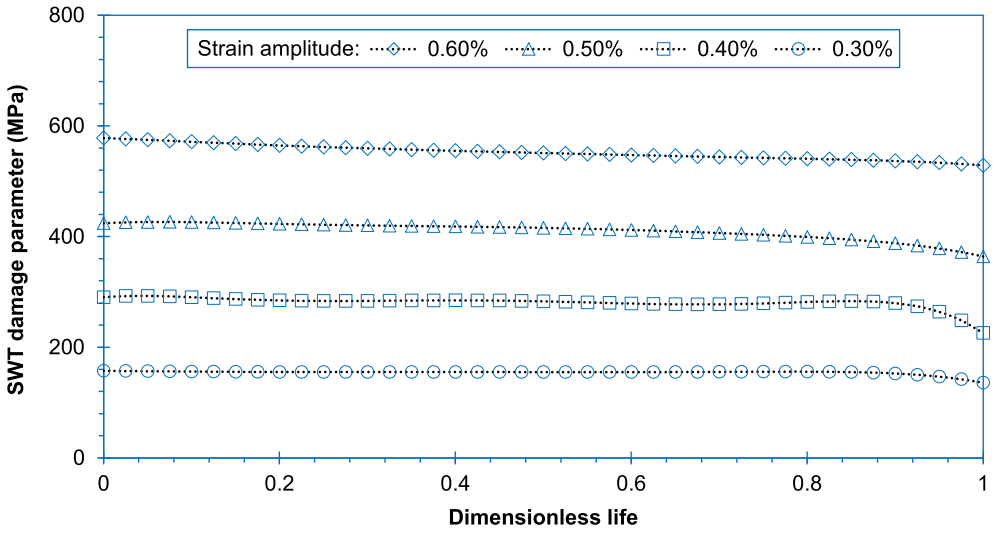

Fig. 13. SWT damage parameter versus dimensionless life at different strain amplitudes for the unixial low-cycle fatigue tests conducted under fully-reversed strain-controlled conditions.

the number of cycles, in a dimensionless form, at different strain amplitudes. As can be seen, this parameter is quite stable throughout the entire lifetime, which is an interesting outcome. Basically, we can distinguish a saturated region, which occupies most of the test, followed by a sudden decrease in the final stage.

Based on the above-mentioned results, the one-parameter fatigue damage law was defined using the mid-life hysteresis loops (see Table 4). The relationship between the SWT damage parameter and the number of cycles to failure computed from the mid-life hysteresis loops for the strain amplitudes tested here is exhibited in Fig. 14. As shown, the data are very well correlated, either at higher or lower strain amplitudes. In a log-log scale, as already reported in the literature, this relationship can be fitted by a straight line [45,76]. The mean curve, represented by the full line, was computed with an high correlation coefficient ($r = 0.993$). Lower and upper bounds (dashed lines) calculated from the mean curve for 5% and 95% failure probabilities were also drawn. The scatter band index is relatively low ($T_{SWT} = 1.302$).

The next step deals with the definition of the material characteristic size (see Eq. (2)) from the fatigue limit stress range ($\Delta\sigma_0$) and the stress intensity factor range threshold (ΔK_{th}). These two variables must be determined under the same stress ratio of the notched component to be assessed. Regarding the former, it was computed from a S–N diagram, defined in terms of nominal stress range versus number of cycles to failure, for pulsating loading conditions. According to Fig. 15, the experimental data are quite close to the fitted function, as demonstrates the high correlation coefficient ($r = 0.986$). For the sake of clarity, 95% confidence bounds for the median curve, given by the ASTM E739 (2015) standard, are also displayed. Here, the fatigue limit stress range is defined as the maximum value at which the specimen can endure 2×10^6 cycles and is equal to 266 MPa.

As far as the stress intensity factor range threshold is concerned, the results obtained from the fatigue crack growth measurements carried out in compact-tension specimens subjected to pulsating loading conditions are shown in Fig. 16. Overall, the scatter is relatively low, either at the threshold area, or at the Paris regime [77]. The threshold value evaluated via the Hartman-Schijve model [78] is equal to 5.2 MPa $\sqrt{m}$. This value is quite close to that reported by Suryawanshi et al. [37] for heat-treated C(T) specimens printed by SLM in the same direction and tested at the same stress ratio (i.e. 5.8 MPa $\sqrt{m}$). Thus, based on the previous values of the stress intensity factor range threshold, and the fatigue limit stress range, the material characteristic size (a_0) for the studied maraging steel is equal to 121.7 μm.

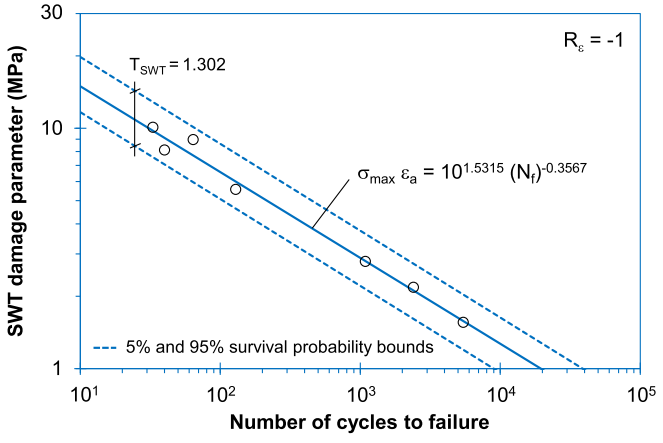

Fig. 14. One-parameter fatigue damage law developed by means of the SWT damage parameter from unixial low-cycle fatigue tests conducted under fully-reversed strain-controlled conditions.

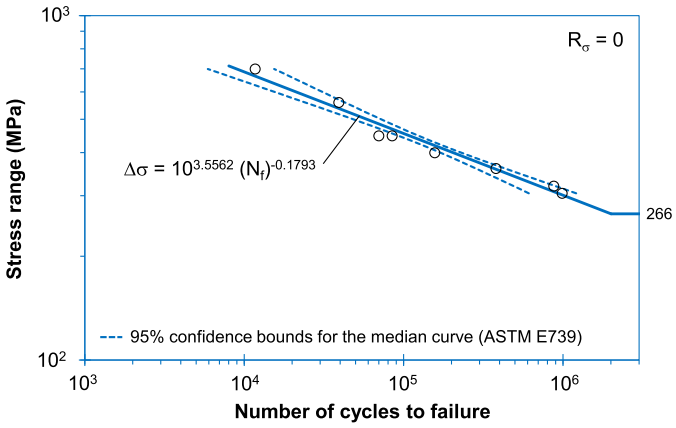

Fig. 15. Stress range against the number of cycles to failure determined from the uniaxial stress-controlled tests.

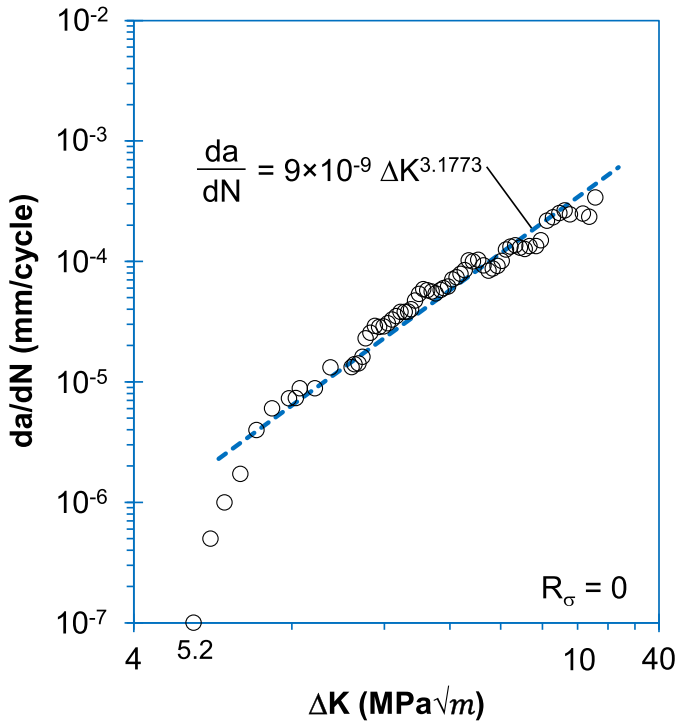

Fig. 16. Fatigue crack growth rates measured under pulsanting loading conditions in compact-tension specimens.

5.3.2. Lifetime prediction

The multiaxial fatigue life of the notched components was calculated using the methodology schematised in Fig. 2. Briefly, the multiaxial loading scenario is reduced to an equivalent uniaxial stress state, which is then used to compute an effective stress range; after that, it is generated a cyclic hysteresis loop allowing the calculation of a representative value of the SWT damage parameter; finally, this value is inserted into a one-parameter damage law to estimate the associated fatigue lifetime. Before testing the predictive capabilities of the proposed concept, it is necessary to obtain the experimental fatigue lives for the different multiaxial loading scenarios.

The experimental fatigue lives were determined from curves relating the surface crack length (a) to the number of cycles (N), termed here a-N curves. Since the fatigue process encompasses the initiation and growth of two cracks, as displayed in Fig. 5, two a-N curves were obtained for each test. Fig. 17 plots typical examples of these curves generated from the measurements carried out for the first crack to appear in the specimen. The data, regardless of the bending-torsion ratio and the nominal stress amplitude, were successfully fitted by exponential functions, represented by the dashed lines. These functions were utilised to determine the fatigue crack initiation life (N_i) considering a crack length equal to the material

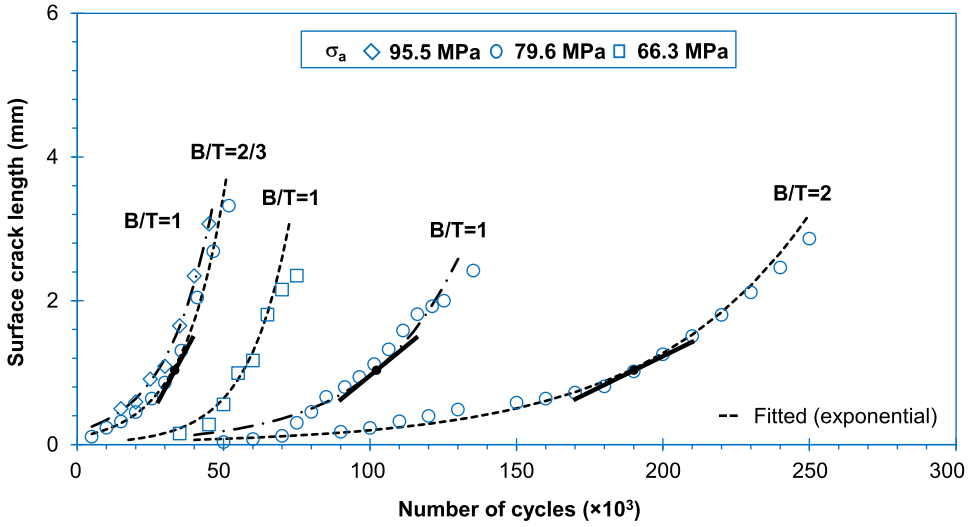

Fig. 17. Crack length versus number of cycles for different multiaxial loading scenarios.

characteristic size (a_0). The values of N_i for the different multiaxial loading scenarios are compiled in Table 3.

Looking at the results, we can conclude that the increase in the B/T ratio leads to smaller fatigue crack growth rates. The analysis of the three curves (circle symbols) with identical nominal normal stress amplitudes ($\sigma_a = 79.6$ MPa) but different bending-torsion ratios clearly demonstrates that the higher the shear stress level, the greater the slope. For the sake of comparability, the slopes for a crack length equal to 1 mm are also displayed in the figure. Another conclusion is that fatigue lives are significantly affected by the stress level. It is clear that the fatigue crack initiation is faster as the nominal stress amplitude climbs. This can be inferred from the three curves plotted for $B/T = 1$, i.e. those identified by the diamonds, squares, and circles.

After the calculation of the experimental lives, we can test the predictive capabilities of the proposed method. Thus, the reduction of the multiaxial stress state to an equivalent uniaxial stress state (see Fig. 2(a)) was done via the von Mises stress. The von Mises stress was computed numerically at the crack initiation site, i.e. at the node with maximum value of the first principal stress (see Fig. 11). Fig. 18 plots the local von Mises stress range ($\Delta\sigma_{vM}$) against the multiaxial fatigue life (N_i) for the different multiaxial loading scenarios. As shown, there is a very good correlation between both variables, which demonstrates the potential of this variable to account for the fatigue damage at the notch-controlled process zone. The potential of the equivalent von Mises stress to deal with notch effects under multiaxial loading has already been reported in the literature [79,80].

Regarding the tests conducted in this research, as displayed in the figure, the data were successfully fitted by a power function (full line) with a high correlation coefficient ($r = 0.998$). Lower and upper bounds (dashed lines) calculated from the mean curve for 5% and 95% failure probabilities were also drawn. The scatter band index was also relatively low ($T_\sigma = 1.208$). Indeed, this value is lower than those found in previous studies conducted under proportional bending-torsion loading in notched geometries made of aluminium alloys and high-strength steels processed by conventional manufacturing [67,68]. We can mention, for instance, the paper by Abreu et al. [82] who found values of T_σ equal to 1.48 and 1.62 for tubular notched and tubular welded geometries, respectively.

The next step of the proposed methodology is the computation of an effective value of $\Delta\sigma_{vM}$ at the initiation region (see Fig. 2(b)). Here, this step was done by applying the line method of the theory of critical distances. The capabilities of the line method in the context of multiaxial fatigue life assessments have been demonstrated in numerous studies [83,84]. Fig. 19 shows the stress distributions determined over a straight line emanating from the fatigue crack

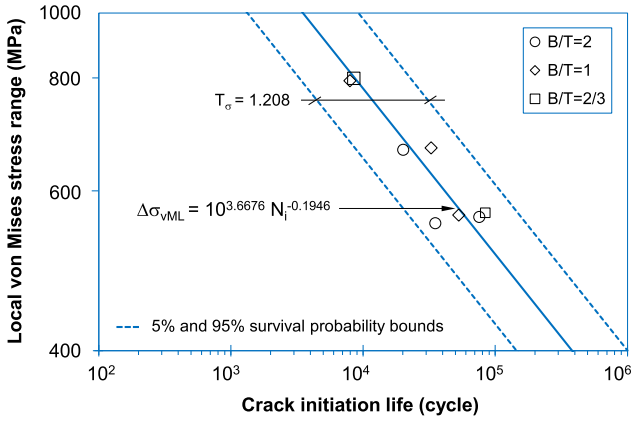

Fig. 18. Relationship between the local von Mises stress range computed at the initiation site versus the number of cycles to crack initiation defined on the basis of the El-Haddad parameter.

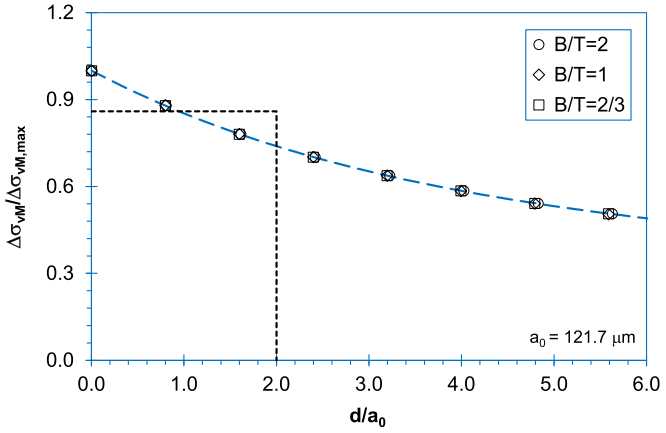

Fig. 19. Evolution of the local von Mises stress range over a straight line emanating from the hole surface, in a dimensionless form, for different multiaxial loading scenarios.

initiation site in the critical direction. In order to simplify the analysis, the local von Mises stress range was divided by the maximum value ($\Delta\sigma_{vM,max}$) and the distance from the hole surface was divided by the material characteristic size (a_0).

The stress distributions near the geometric discontinuity, as shown in Fig. 19, are maximum at the surface and then progressively reduce to an asymptotic value, which is compatible with a linear-elastic analysis. On the other hand, despite the differences regarding the loading scenario, dimensionless curves are perfectly overlapped. Based on these curves, we can conclude that the effective value of the local von Mises stress range ($\Delta\sigma_{vM,eff}$) computed by the line method is equal to 86% of the maximum local stress. Some local unsensitivity to the loading scenario has been observed by Branco et al. [83] in the dimensionless stress distributions for solid round bars with lateral notches and transverse blind holes subjected to in-phase bending-torsion, particularly when the distance from the crack initiation site, in a direction normal to notch surface normalised by the material characteristic length (d/a_0) was smaller than 1.

The computation of an average local von Mises stress range allows the generation of a cyclic hysteresis loop (see Fig. 2(c)) which can be used to calculate a representative value of the SWT damage parameter at the fatigue process zone. In this study, the equivalent strain energy density concept (ESED) proposed by Glinka et al. [85], and the improved equivalent strain energy density concept (iESED) developed by Ye et al. [86] were used for this purpose. A detailed review about the mathematical background and the physical meaning of the two above-mentioned concepts can be found in the paper by Liao et al. [61].

Typical hysteresis loops obtained from both methods for the same multiaxial loading case ($B/T = 2/3$) are exhibited in Fig. 20. As far as we can see, the differences are not particularly expressive, either the maximum stresses or the strain amplitudes are quite similar. According to the figure, the amount of plastic deformation is relatively small (not only in the case displayed, but also in all cases analysed in this research). Once the generation of the cyclic hysteresis loops is completed, representative values of the SWT damage parameter associated with the different loading scenarios can be determined, as well as the corresponding multiaxial fatigue lifetime (see Fig. 2(d)). The predicted lives, estimated by means of the ESED (N_p^{ESED}) and iESED (N_p^{iESED}) concepts, are listed in Table 6.

Fig. 21 plots the experimental fatigue lives (N_i) against the predicted lives (N_p) for the two approaches studied here. In order to simplify the analysis, conservative and non-conservative scatter bounds with factors of two (i.e. $N_i = 2N_p$ and $N_p = 2N_i$) were drawn. Overall, the predictive capabilities of the proposed approaches are remarkable. In both cases, there is a strong correlation between the data, with all points within

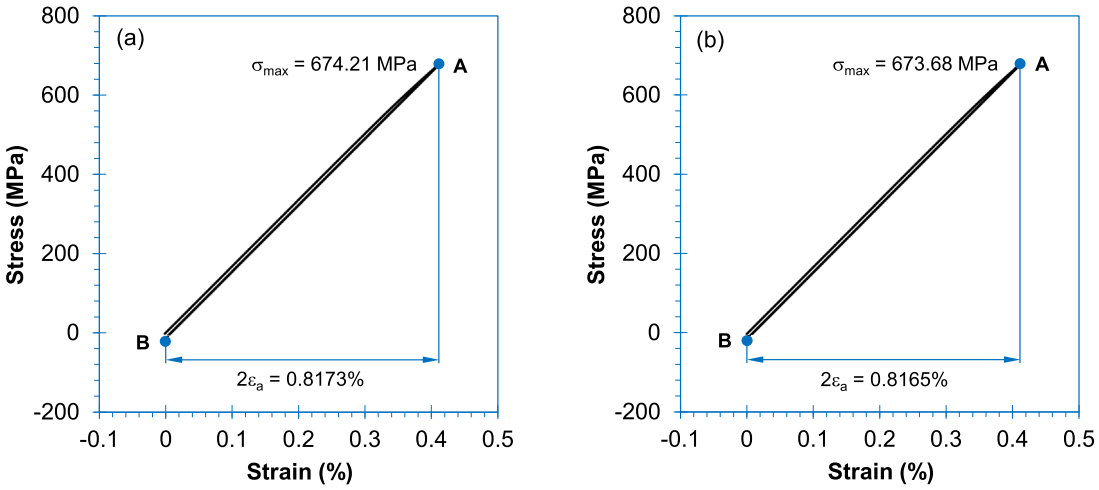

Fig. 20. Cyclic stress-strain loops generated from the effective von Mises stress range using the: (a) equivalent strain energy density; and (b) improved equivalent strain energy density concepts for B/T = 2/3.

Table 6
Summary of predicted lives for the multiaxial fatigue tests.

B/T	2	2	2	1	1	1	2/3	2/3
N_i (cycles)	35,115	75,516	20,037	52,883	32,677	7947	84,204	8514
N_p^{ESED} (cycles)	60,877	55,430	20,179	54,154	19,719	7418	52,310	8097
N_p^{iESED} (cycles)	60,866	55,420	20,164	54,143	19,703	7398	52,303	8080

the delimited area. This clearly demonstrates the robustness of the proposed methodology. A close look at the figure shows a mixed behaviour, i.e. predicted lives are either conservative or non-conservative. Regarding the two methods used to account for the cyclic plasticity at the notch, no relevant differences were found for this material.

In order to quantitatively analyse the predictive capabilities of the proposed approaches, a statistical study based on the fatigue life prediction error (E_N), given by the following formula, was conducted:

$$E_N = \log_{10}\left(\frac{N_i}{N_p}\right) \tag{4}$$

where N_i is the experimental life, and N_p is the predicted life. Fig. 22 shows the probability density functions obtained for the ESED and the iESED concepts. As far as we can see, the two functions are similar, showing identical mean errors and identical standard deviations. Furthermore, both approaches tend to be conservative, which is an interesting outcome.

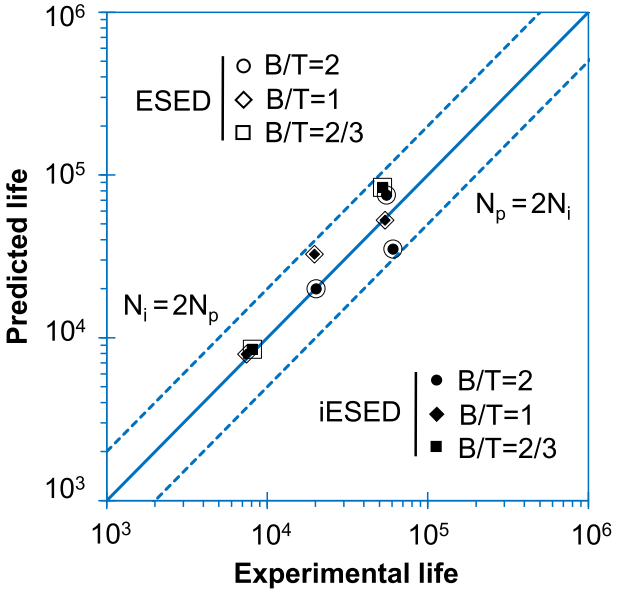

Fig. 21. Predicted lives versus experimental lives for the proposed method using both the equivalent strain energy density (ESED) and the improved equivalent strain energy density (iESED) concepts.

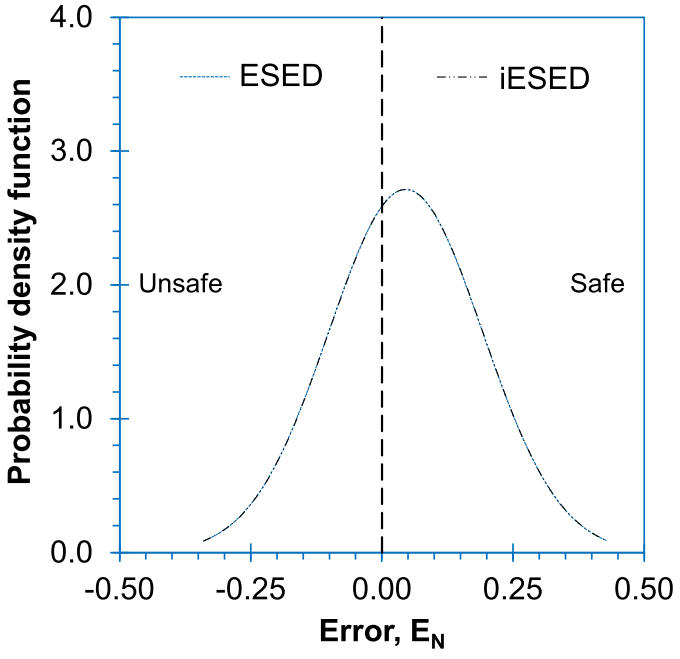

Fig. 22. Probability density functions for the multiaxial fatigue life predictions obtained with the equivalent strain energy density (ESED) and the improved equivalent strain energy density (iESED) concepts.

6. Conclusions

The present paper studied the multiaxial fatigue behaviour of maraging steels produced by selective laser melting. Multiaxial fatigue tests were conducted in hollow cylindrical bars with transverse circular holes under in-phase bending-torsion loading. Complementary, low-cycle fatigue tests, high-cycle fatigue tests, and fatigue crack growth tests under uniaxial loading conditions were performed to characterise the material behaviour and to develop a one-parameter fatigue damage law. Finally, within a linear-elastic framework, it was developed a straightforward approach to predict the multiaxial fatigue lifetime. The following conclusions can be drawn:

- fatigue failure was characterised by the initiation and growth of two cracks at diametrically opposite sites around the hole surface. Unmelted regions at the surface and sub-surface, resulting from insufficient fusion or inadequate penetration, were the main cause of fatigue crack initiation;
- fatigue crack initiation sites and fatigue crack angles at the early stage of growth were governed by the loading scenario. These variables were successfully predicted from the maximum value of the first principal stress and from the first principal direction at the initiation site, respectively;
- the reduction of the multiaxial stress state to an uniaxial stress state, via the equivalent von Mises stress evaluated at the fatigue crack initiation region, was adequate to correlate the loading scenario with the number of cycles to failure in notched components subjected to in-phase bending-torsion loading;
- an effective value of the SWT damage parameter, defined from a cyclic hysteresis loop generated by combining a notch-plasticity correction rule, namely the ESED or the IESED, with the theory of critical distances was able to characterise the fatigue damage at the notch-controlled process zone;
- the proposed fatigue life prediction model, built up with a reduced number of material constants and supported by a linear-elastic framework, is particularly suitable for industrial applications as well as to deal with maraging steel components subjected to proportional multiaxial loading.

Data availability

The raw/processed data required to reproduce these findings cannot be shared at this time due to technical or time limitations.

credit author statement missing

Conceptualization: R. Branco, J.D. Costa Funding: J.A. Martins Ferreira, C. Capela Investigation: R. Branco, J.D. Costa, W. Macek Visualization: R. Branco, W. Macek, F.V. Antunes Writing (original draft): R. Branco Writing (review & editing): R. Branco, J.D. Costa, J.A. Martins Ferreira, C. Capela, F.V. Antunes, W. Macek

Declaration of Competing Interest

The authors declare that they have no known competing financial interests or personal relationships that could have appeared to influence the work reported in this paper.

Acknowledgement

This research is sponsored by FEDER funds through the program COMPETE – Programa Operacional Factores de Competitividade – and by national funds through FCT – Fundação para a Ciência e a Tecnologia –, under the project UIDB/00285/2020. The authors would like to acknowledge the sponsoring under the project number 016713 (PTDC/EMS-PRO/1356/2014) financed by Project 3599 Promover a Produção Científica e Desenvolvimento Tecnológico e a Constituição de Redes Temáticas (3599-PPCDT) and FEDER funds and also EROFIO S.A. industry for the supply of the testing samples. The authors are thankful to the master student Daniel Monteiro.

References

[1] K. Kempen, E. Yasa, L. Thijs, J.P. Kruth, J. Van Humbeeck, Microstructure and mechanical properties of selective laser melted 18Ni-300 steel, Phys. Procedia (2011) https://doi.org/10.1016/j.phpro.2011.03.033.
[2] P. Kürnsteiner, M.B. Wilms, A. Weisheit, P. Barriobero-Vila, E.A. Jägle, D. Raabe, Massive nanoprecipitation in an Fe-19Ni-xAl maraging steel triggered by the intrinsic heat treatment during laser metal deposition, Acta Mater. (2017)https://doi.org/10.1016/j.actamat.2017.02.069.
[3] B. Mooney, K.I. Kourousis, R. Raghavendra, Plastic anisotropy of additively manufactured maraging steel: influence of the build orientation and heat treatments, Addit Manuf. (2019)https://doi.org/10.1016/j.addma.2018.10.032.
[4] C. Tan, K. Zhou, W. Ma, P. Zhang, M. Liu, T. Kuang, Microstructural evolution, nanoprecipitation behavior and mechanical properties of selective laser melted high-performance grade 300 maraging steel, Mater. Des. (2017)https://doi.org/10.1016/j.matdes.2017.08.026.
[5] E.A. Jägle, P.P. Choi, J. Van Humbeeck, D. Raabe, Precipitation and austenite reversion behavior of a maraging steel produced by selective laser melting, J. Mater. Res. (2014)https://doi.org/10.1557/jmr.2014.204.
[6] A. Suzuki, R. Nishida, N. Takata, M. Kobashi, M. Kato, Design of laser parameters for selectively laser melted maraging steel based on deposited energy density, Addit Manuf. (2019)https://doi.org/10.1016/j.addma.2019.04.018.
[7] H. Fayazfar, M. Salarian, A. Rogalsky, et al., A critical review of powder-based additive manufacturing of ferrous alloys: process parameters, microstructure and mechanical properties, Mater. Des. (2018)https://doi.org/10.1016/j.matdes.2018.02.018.
[8] P. Bajaj, A. Hariharan, A. Kini, P. Kürnsteiner, D. Raabe, E.A. Jägle, Steels in additive manufacturing: a review of their microstructure and properties, Mater. Sci. Eng. A (2020)https://doi.org/10.1016/j.msea.2019.138633.
[9] B. Mooney, K. Kourousis, A review of factors affecting the mechanical properties of maraging steel 300 fabricated via laser powder bed fusion, Metals (Basel) (2020) https://doi.org/10.3390/met10091273.
[10] K. Monkova, I. Zetkova, L. Kučerová, M. Zetek, P. Monka, M. Daňa, Study of 3D printing direction and effects of heat treatment on mechanical properties of MS1 maraging steel, Arch. Appl. Mech. (2019)https://doi.org/10.1007/s00419-018-1389-3.
[11] B. Mooney, K.I. Kourousis, R. Raghavendra, D. Agius, Process phenomena influencing the tensile and anisotropic characteristics of additively manufactured maraging steel, Mater. Sci. Eng. A (2019)https://doi.org/10.1016/j.msea.2018.12.070.
[12] G. Casalino, S.L. Campanelli, N. Contuzzi, A.D. Ludovico, Experimental investigation and statistical optimisation of the selective laser melting process of a maraging steel, Opt. Laser Technol. (2015)https://doi.org/10.1016/j.optlastec.2014.07.021.
[13] Y. Bai, Y. Yang, D. Wang, M. Zhang, Influence mechanism of parameters process and mechanical properties evolution mechanism of maraging steel 300 by selective laser melting, Mater. Sci. Eng. A (2017)https://doi.org/10.1016/j.msea.2017.06.033.
[14] S. Wei, G. Wang, L. Wang, Y. Rong, Characteristics of microstructure and stresses and their effects on interfacial fracture behavior for laser-deposited maraging steel, Mater. Des. (2018)https://doi.org/10.1016/j.matdes.2017.10.020.
[15] S. Shamsdini, M. Ghoncheh, M. Mohammadi, Plastic deformation throughout strain-induced phase transformation in additively manufactured maraging steels, Mater. Des. (2020)https://doi.org/10.1016/j.matdes.2020.109289.
[16] F.F. Conde, J.D. Escobar, J.P. Oliveira, et al., Effect of thermal cycling and aging stages on the microstructure and bending strength of a selective laser melted 300-grade maraging steel, Mater. Sci. Eng. A (2019)https://doi.org/10.1016/j.msea.2019.03.129.
[17] M. Majeed, M. Vural, S. Raja, M. Shaikh, Finite element analysis of thermal behavior in maraging steel during SLM process, Optik (2020)https://doi.org/10.1016/j.ijleo.2019.164128.
[18] R. Casati, J. Lemke, A. Tuissi, M. Vedani, Aging behaviour and mechanical performance of 18-ni 300 steel processed by selective laser melting, Metals (Basel) (2016)https://doi.org/10.3390/met6090218.
[19] J. Mutua, S. Nakata, T. Onda, Z.C. Chen, Optimization of selective laser melting parameters and influence of post heat treatment on microstructure and mechanical properties of maraging steel, Mater. Des. (2018)https://doi.org/10.1016/j.matdes.2017.11.042.
[20] W. Wu, X. Wang, Q. Wang, J. Liu, Y. Zhang, T. Hua, P. Jiang, Microstructure and mechanical properties of maraging 18Ni-300 steel obtained by powder bed based selective laser melting process, Rapid Prototyp. J. (2020)https://doi.org/10.1108/RPJ-08-2018-0189.
[21] T. Bhardwaj, M. Shukla, Effect of laser scanning strategies on texture, physical and mechanical properties of laser sintered maraging steel, Mater. Sci. Eng. A (2018) https://doi.org/10.1016/j.msea.2018.07.089.
[22] Z.C. Oter, Y. Gencer, M. Tarakci, Microstructure evolution and surface quality of laser-sintered maraging steel parts produced on different building platform positions, Optik (Stuttg) (2020)https://doi.org/10.1016/j.ijleo.2019.163568.
[23] S. Dehgahi, A. Hadadzadeh, M.H. Ghoncheh, H. Sanjari, B. Shalchi Amirkhiz, M. Mohammadi, The role of titanium on the microstructure and mechanical properties of additively manufactured C300 Maraging steels, Mater. Des. (2020)https://doi.org/10.1016/j.matdes.2020.108965.
[24] D. Croccolo, M. De Agostinis, S. Fini, G. Olmi, A. Vranic, S. Ciric-Kostic, Influence of the build orientation on the fatigue strength of EOS maraging steel produced by additive metal machine, Fatigue Fract. Eng. Mater. Struct. (2016)https://doi.org/10.1111/ffe.12395.

[25] D. Croccolo, M. De Agostinis, S. Fini, et al., Fatigue response of as-built DMLS maraging steel and effects of aging, machining, and peening treatments, Metals (Basel) (2018)https://doi.org/10.3390/met8070505.

[26] D. Croccolo, M. De Agostinis, S. Fini, et al., Sensitivity of direct metal laser sintering Maraging steel fatigue strength to build orientation and allowance for machining, Fatigue Fract. Eng. Mater. Struct. (2019)https://doi.org/10.1111/ffe.12917.

[27] D. Croccolo, M. De Agostinis, S. Fini, et al., Experimental study on the sensitivity of DMLS manufactured maraging steel fatigue strength to the build orientation and allowance for machining, Proc IRF2018 6th Int Conf Integrity-Reliability-Failure, 2018.

[28] D. Croccolo, M. De Agostinis, S. Fini, et al., Effects of machining and heat and surface treatments on as built dmls processed maraging steel, Struct. Integrity (2019) https://doi.org/10.1007/978-3-319-91989-8_24.

[29] C. Elangeswaran, K. Gurung, R. Koch, A. Cutolo, B. Hooreweder, Post-treatment selection for tailored fatigue performance of 18Ni300 maraging steel manufactured by laser powder bed fusion, Fatigue Fract. Eng. Mater. Struct. (2020)https://doi.org/10.1111/ffe.13304.

[30] E. Bouzakis, A. Arvanitidis, F. Kazelis, G. Maliaris, N. Michailidis, Comparison of additively manufactured vs. conventional maraging steel in corrosion-fatigue performance after various surface treatments, Procedia CIRP (2020)https://doi.org/10.1016/j.procir.2020.03.003.

[31] J.A.M. Ferreira, L.M.S. Santos, J. Da Silva, J.M. Costa, C. Capela, Assessment of the fatigue life on functional hybrid laser sintering steel components, Procedia Struct. Integrity (2016)https://doi.org/10.1016/j.prostr.2016.02.018.

[32] L.M.S. Santos, J.A.M. Ferreira, J.S. Jesus, J.M. Costa, C. Capela, Fatigue behaviour of selective laser melting steel components, Theor. Appl. Fract. Mech. (2016)https://doi.org/10.1016/j.tafmec.2016.08.011.

[33] L.M.S. Santos, J.A.M. Ferreira, J.D. Costa, C. Capela, Fatigue performance of hybrid steel samples with laser sintered implants, Procedia Eng. (2016)https://doi.org/10.1016/j.proeng.2016.08.874.

[34] L.M.S. Santos, L.P. Borrego, J.A.M. Ferreira, J. de Jesus, J.D. Costa, C. Capela, Effect of heat treatment on the fatigue crack growth behaviour in additive manufactured AISI 18Ni300 steel, Theor. Appl. Fract. Mech. (2019)https://doi.org/10.1016/j.tafmec.2019.04.005.

[35] L. Santos, J. Ferreira, L. Borrego, J. Costa, C. Capela, J. Jesus, Fatigue crack propagation along interfaces of selective laser, Fatigue Fract. Eng. Mater. Struct. (2019)https://doi.org/10.1111/ffe.13072.

[36] J. Suryawanshi, K.G. Prashanth, U. Ramamurty, Tensile, fracture, and fatigue crack growth properties of a 3D printed maraging steel through selective laser melting, J. Alloys Compd. (2017)https://doi.org/10.1016/j.jallcom.2017.07.177.

[37] G. Meneghetti, D. Rigon, C. Gennari, An analysis of defects influence on axial fatigue strength of maraging steel specimens produced by additive manufacturing, Int. J. Fatigue (2019)https://doi.org/10.1016/j.ijfatigue.2018.08.034.

[38] G. Meneghetti, D. Rigon, D. Cozzi, W. Waldhauser, M. Dabalà, Influence of build orientation on static and axial fatigue properties of maraging steel specimens produced by additive manufacturing, Procedia Struct. Integrity (2017)https://doi.org/10.1016/j.prostr.2017.11.072.

[39] J. Damon, T. Hanemann, S. Dietrich, G. Graf, K.H. Lang, V. Schulze, Orientation dependent fatigue performance and mechanisms of selective laser melted maraging steel X3NiCoMoTi18-9-5, Int. J. Fatigue (2019)https://doi.org/10.1016/j.ijfatigue.2019.06.025.

[40] A. Gatto, E. Bassoli, L. Denti, Repercussions of powder contamination on the fatigue life of additive manufactured maraging steel, Addit Manuf. (2018)https://doi.org/10.1016/j.addma.2018.09.004.

[41] L.M.S. Santos, C. Capela, F.V. Antunes, Ferreira JAM, J.D. Costa, R. Branco, A novel specimen geometry for fatigue crack growth in vacuum, Lecture Notes in Mechanical Engineering, 2020https://doi.org/10.1007/978-3-030-29041-2_27.

[42] C. Douellou, X. Balandraud, E. Duc, B. Verquin, F. Lefebvre, F. Sar, Fast fatigue characterization by infrared thermography for additive manufacturing, Procedia Struct. Integrity (2019)https://doi.org/10.1016/j.prostr.2019.12.011.

[43] C. Douellou, X. Balandraud, E. Duc, B. Verquin, F. Lefebvre, F. Sar, Rapid characterization of the fatigue limit of additive-manufactured maraging steels using infrared measurements, Addit Manuf. (2020)https://doi.org/10.1016/j.addma.2020.101310.

[44] R. Branco, J. Silva, J.M. Ferreira, et al., Fatigue behaviour of maraging steel samples produced by SLM under constant and variable amplitude loading, Procedia Struct. Integrity (2019)https://doi.org/10.1016/j.prostr.2020.01.002.

[45] L. Santos, R. Branco, J.D. Costa, C. Capela, J.A. Martins Ferreira, Fatigue life prediction in selective laser melted samples under variable amplitude loading based on two constant-amplitude tests, Lecture Notes in Mechanical Engineering, 2020https://doi.org/10.1007/978-3-030-29041-2_28.

[46] R. Branco, J.D.M. Costa, F. Berto, et al., Low-cycle fatigue behaviour of AISI 18Ni300 maraging steel produced by selective laser melting, Metals (Basel) 8 (1) (2018) https://doi.org/10.3390/met8010032.

[47] B. Mooney, D. Agius, K.I. Kourousis, Cyclic plasticity of the as-built EOS Maraging steel: preliminary experimental and computational results, Appl. Sci. (2020) https://doi.org/10.3390/app10041232.

[48] F. Antunes, L. Santos, C. Capela, et al., Fatigue crack growth in maraging steel obtained by selective laser melting, Appl. Sci. (2019)https://doi.org/10.3390/app9204412.

[49] B. Marques, L.P. Borrego, J.M. Ferreira, F.V. Antunes, R. Branco, A numerical analysis of fatigue crack closure using CTOD, Procedia Struct. Integrity (2019)https://doi.org/10.1016/j.prostr.2019.08.211.

[50] L.F.P. Borrego, F.V. Antunes, Ferreira JAM, J.D. Costa, C. Capela, Analysis of fatigue crack propagation in laser sintering metal, Procedia Struct. Integrity (2017)https://doi.org/10.1016/j.prostr.2017.07.123.

[51] F.V. Antunes, M.F. Borges, B. Marques, P. Prates, R. Branco, Crack tip mechanisms: a numerical analysis, Procedia Struct. Integrity (2019)https://doi.org/10.1016/j.prostr.2020.01.147.

[52] A. Ebrahimi, M. Mohammadi, Numerical tools to investigate mechanical and fatigue properties of additively manufactured MS1-H13 hybrid steels, Addit Manuf. (2018) https://doi.org/10.1016/j.addma.2018.07.009.

[53] S. Afkhami, M. Dabiri, S.H. Alavi, T. Björk, A. Salminen, Fatigue characteristics of steels manufactured by selective laser melting, Int. J. Fatigue (2019)https://doi.org/10.1016/j.ijfatigue.2018.12.029.

[54] D. Socie, G. Marquis, Multiaxial Fatigue, Society of Automotive Engineers, Warrendale, PA, 2000.

[55] F. Berto, P. Lazzarin, C. Marangon, Fatigue strength of notched specimens made of 40CrMoV13.9 under multiaxial loading, Mater. Des. (2014)https://doi.org/10.1016/j.matdes.2013.08.013.

[56] S.P. Zhu, Y. Liu, Q. Liu, Z.Y. Yu, Strain energy gradient-based LCF life prediction of turbine discs using critical distance concept, Int. J. Fatigue (2018)https://doi.org/10.1016/j.ijfatigue.2018.04.006.

[57] A. Carpinteri, A. Spagnoli, Multiaxial high-cycle fatigue criterion for hard metals, Int. J. Fatigue (2001)https://doi.org/10.1016/S0142-1123(00)00075-X.

[58] A. Tadesse, S.P. Zhu, D. Liao, B. Keshtegar, Cyclic plastic zone-based notch analysis and damage evolution model for fatigue life prediction of metals, Mater. Des. (2020)https://doi.org/10.1016/j.matdes.2020.108639.

[59] S.P. Zhu, J.C. He, D. Liao, Q. Wang, Y. Liu, The effect of notch size on critical distance and fatigue life predictions, Mater. Des. (2020)https://doi.org/10.1016/j.matdes.2020.109095.

[60] D. Liao, S.P. Zhu, J.A.F.O. Correia, A.M.P. De Jesus, F. Berto, Recent advances on notch effects in metal fatigue: a review, Fatigue Fract. Eng. Mater. Struct. (2020)https://doi.org/10.1111/ffe.13195.

[61] J. Correia, N. Apetre, A. Arcari, et al., Generalized probabilistic model allowing for various fatigue damage variables, Int. J. Fatigue (2017)https://doi.org/10.1016/j.ijfatigue.2017.03.031.

[62] M.H. El Haddad, T.H. Topper, K.N. Smith, Prediction of non propagating cracks, Eng. Fract. Mech. (1979)https://doi.org/10.1016/0013-7944(79)90081-X.

[63] D. Taylor, Geometrical effects in fatigue: a unifying theoretical model, Int. J. Fatigue (1999)https://doi.org/10.1016/S0142-1123(99)00007-9.

[64] D. Taylor, The theory of critical distances: a link to micromechanisms, Theor. Appl. Fract. Mech. (2017)https://doi.org/10.1016/j.tafmec.2017.05.018.

[65] L. Newton, N. Senin, C. Gomez, R. Danzl, F. Helmli, L. Blunt, et al., Areal topography measurement of metal additive surfaces using focus variation microscopy, Addit Manuf. (2019)https://doi.org/10.1016/j.addma.2018.11.013.

[66] W. Macek, R. Owsiński, J. Trembacz, R. Branco, Three-dimensional fractographic analysis of total fracture areas in 6082 aluminium alloy specimens under fatigue bending with controlled damage degree, Mech. Mater. (2020)https://doi.org/10.1016/j.mechmat.2020.103410.

[67] P. Luo, W. Yao, L. Susmel, P. Li, Prediction methods of fatigue critical point for notched components under multiaxial fatigue loading, Fatigue Fract. Eng. Mater. Struct. (2019)https://doi.org/10.1111/ffe.13116.

[68] M. de Freitas, Multiaxial fatigue: from materials testing to life prediction, Theor. Appl. Fract. Mech. (2017)https://doi.org/10.1016/j.tafmec.2017.05.008.

[69] P. Lopez-Crespo, B. Moreno, A. Lopez-Moreno, J. Zapatero, Study of crack orientation and fatigue life prediction in biaxial fatigue with critical plane models, Eng. Fract. Mech. (2015)https://doi.org/10.1016/j.engfracmech.2015.01.020.

[70] D. Rozumek, Z. Marciniak, Fatigue crack growth in AlCu4Mg1 under nonproportional bending with torsion loading, Mater. Sci. (2011)https://doi.org/10.1007/s11003-011-9341-5.

[71] D. Rozumek, Z. Marciniak, G. Lesiuk, J.A.F.O. Correia, A.M.P. De Jesus, Experimental and numerical investigation of mixed mode I+II and I+III fatigue crack growth in S355J0 steel, Int. J. Fatigue (2018)https://doi.org/10.1016/j.ijfatigue.2018.04.005.

[72] P. Zerres, J. Brüning, M. Vormwald, Fatigue crack growth behavior of fine-grained steel S460N under proportional and non-proportional loading, Eng. Fract. Mech. (2010)https://doi.org/10.1016/j.engfracmech.2010.02.008.

[73] R. Branco, J.D. Costa, F.V. Antunes, Fatigue behaviour and life prediction of lateral notched round bars under bending-torsion loading, Eng. Fract. Mech. 119 (2014) https://doi.org/10.1016/j.engfracmech.2014.02.009.

[74] M. Kahlin, H. Ansell, D. Basu, A. Kerwin, L. Newton, B. Smith, et al., Improved fatigue strength of additively manufactured Ti6Al4V by surface post processing, Int. J. Fatigue (2020)https://doi.org/10.1016/j.ijfatigue.2020.105497.

[75] W. Macek, R. Branco, J. Trembacz, J.D. Costa, J.A.M. Ferreira, C. Capela, Effect of multiaxial bending-torsion loading on fracture surface parameters in high-strength steels processed by conventional and additive manufacturing, Eng. Fail. Anal. (2020)https://doi.org/10.1016/j.engfailanal.2020.104784.

[76] S. Kwofie, An exponential stress function for predicting fatigue strength and life due to mean stresses, Int. J. Fatigue (2001)https://doi.org/10.1016/S0142-1123(01)00044-5.

[77] P.C. Paris, F. Erdogan, A critical analysis of crack propagations laws, J. Basic Eng. (1963)https://doi.org/10.1115/1.3656900.

[78] A. Hartman, J. Schijve, The effects of environment and load frequency on the crack propagation law for macro fatigue crack growth in aluminium alloys, Eng. Fract. Mech. (1970)https://doi.org/10.1016/0013-7944(70)90003-2.

[79] D.H. Li, D.G. Shang, L. Xue, L.J. Li, L.W. Wang, J. Cui, Notch stress-strain estimation method based on pseudo stress correction under multiaxial thermo-mechanical cyclic loading, Int. J. Solids Struct. (2020)https://doi.org/10.1016/j.ijsolstr.2020.04.002.

[80] R. Branco, P.A. Prates, J.D. Costa, F. Berto, A. Kotousov, New methodology of fatigue life evaluation for multiaxially loaded notched components based on two uniaxial strain-controlled tests, Int. J. Fatigue 111 (2018)https://doi.org/10.1016/j.ijfatigue.2018.02.027.

[81] L.M.P. Abreu, J.D. Costa, J.A.M. Ferreira, Fatigue behaviour of AlMgSi tubular specimens subjected to bending-torsion loading, Int. J. Fatigue (2009)https://doi.org/10.1016/j.ijfatigue.2009.03.004.

[82] R. Branco, J.D. Costa, F. Berto, A. Kotousov, F.V. Antunes, Fatigue crack initiation behaviour of notched 34CrNiMo6 steel bars under proportional bending-torsion loading, Int. J. Fatigue (2020)https://doi.org/10.1016/j.ijfatigue.2019.105268.

[83] Z. Hu, F. Berto, Y. Hong, L. Susmel, Comparison of TCD and SED methods in fatigue lifetime assessment, Int. J. Fatigue (2019)https://doi.org/10.1016/j.ijfatigue.2019.02.009.

[84] G. Glinka, W. Ott, H. Nowack, Elastoplastic plane strain analysis of stresses and strains at the notch root, J. Eng. Mater. Technol. (1988)https://doi.org/10.1115/1.3226037.

[85] D.Y. Ye, S. Matsuoka, N. Suzuki, Y. Maeda, Further investigation of Neuber's rule and the equivalent strain energy density (ESED) method, Int. J. Fatigue (2004)https://doi.org/10.1016/j.ijfatigue.2003.10.002.